ABSTRACT

Title of Thesis: MEASUREMENT OF BEAM SECTIONAL STIFFNESS PROPERTIES

Sheng-Wei Wang
Master of Science, 2019

Thesis Directed By: Professor Olivier A. Bauchau
Department of Aerospace Engineering

Among all strain measurement techniques, digital image correlation is preferred over others because of its versatility, high accuracy and ability to produce full-field strain maps. The sectional stiffness properties of beams with simple configuration and made of homogeneous materials can be evaluated easily based on simple formulas. For aerospace applications, beams such as helicopter rotor blades present complex geometries and are made of heterogeneous, anisotropic composite materials. Evaluation of the sectional stiffness properties is an arduous task that requires a finite element based analysis of the cross-section. This thesis presents an approach that combines experimental measurements based on digital image correlation with a finite element model of the beam's cross-section to measure its sectional stiffness properties. The proposed approach is able to deal with rotor blades presenting arbitrary cross-sectional configuration made of anisotropic composite materials.

MEASUREMENT OF BEAM SECTIONAL STIFFNESS PROPERTIES

by

Sheng-Wei Wang

Thesis submitted to the Faculty of the Graduate School of the
University of Maryland, College Park in partial fulfillment
of the requirements for the degree of
Master of Science
2019

Advisory Committee:
Professor Olivier A. Bauchau, Chair/Advisor
Professor Inderjit Chopra
Professor Sung W. Lee

Acknowledgments

My very first and foremost gratitude goes to my advisor, Prof. Olivier Bauchau, for his consistent guidance and enlightenment throughout this entire progress of studying and researching. His unparalleled knowledge and kindness are what I have been grateful for.

I also want to show my great thankfulness to Prof. Chopra and Prof. Lee for their advice and support as my committee members.

My gratefulness to my dearest wife and both families are beyond words. Thank you so much for always backing me up in every single difficult time and keeping my world dynamic.

Additionally, I want to thank Tyler Sinotte, my partner on this project, for his resourcefulness to see me through every time I hit a bottle neck. Also, the genuine happiness I share with all labmates (Valentin, Alfonso, Tyler, Shilei, Nishant, Matteo, Minghe and Giuseppe) is truly an epic treasure. Thank you all for both technical and mental support on this journey.

Moreover, I want to thank my sponsor, NDU in Taiwan, for the assistance on my master's degree. Had it not been for their support, my dream could have never been this solid.

Finally, I thank all the individuals around me and thank God for making these invaluable episodes happen in my life.

Table of Contents

List of Tables

List of Figures

Chapter 1: Introduction

This chapter outlines the objective of this thesis. A brief review of the methods used measure strain fields follows; both contacting and non-contacting methods are presented and their respective strengths and weaknesses are underlined. Next, the approaches that have been used to measure the sectional stiffness characteristics of rotor blades are summarized and the deficiencies of these approaches are underlined. Finally, an approach is proposed that has the potential to provide accurate measurements of the sectional stiffness characteristics of helicopter rotor blades.

1.1 Motivation and Objective

The design of helicopter rotor blades requires extensive analysis of its dynamic response, typically using comprehensive analysis tools. In these codes, beam theory is used to model the rotor blade, and hence, the sectional stiffness and mass properties of the blade must be known to perform the analysis. Because these blades are made of anisotropic composite materials and present complex cross-sectional geometries, this task is rather arduous. Yet, these sectional characteristics play a key role in the analysis as they impact *(1)* rotor dynamics, *(2)* blade elastic couplings, and *(3)* the resulting stress and strain fields in operation.

Sectional stiffness characteristics can be evaluated easily within the framework of engineering beam theories. For instance, Euler-Bernoulli beam theory [4] provides a closed-form formula for the beam's sectional axial and bending stiffnesses. When it comes to torsion, Saint-Venant's theory [4] provides a solution of the problem but requires the solution of Poisson's equation over the beam's cross-sectional domain. When dealing with realistic helicopter rotor blades made of anisotropic composite materials and presenting complex cross-sectional geometries, these approaches are inadequate because the assumptions on which they are based are no longer applicable. Furthermore, these theories are unable to evaluate the complete six-by-six sectional stiffness matrix that captures all the elastic coupling effect resulting from the use of composite materials.

In view of these difficulties, experimental measurement of the sectional stiffness properties appears to be desirable. In most cases, these approaches assume that the beam present uniform properties along its span. Clearly, these approaches are flawed because *(1)* they are incapable of measuring full six-by-six stiffness matrix, *(2)* are unable to detect high strain gradients, and *(3)* providing only average, rather than local, structural stiffness properties.

The objective of this thesis is to present an experimental techniques that will overcome the above deficiencies. The proposed method aims to measure the complete six-by-six stiffness matrix of helicopter rotor blades made of advanced composite material and presenting arbitrary configurations. The goal of the thesis is to establish the soundness of the proposed approach and to develop the data reduction procedure. The development of the actual instrumentation is beyond the scope of

this work.

This chapter present a review of the various techniques used to measure *(1)* beam sectional stiffness properties and *(2)* strain fields.

1.2 Review of Stiffness Measurement Methodology

This section presents a review of the simple approaches used to measure the sectional stiffness properties of beams. Typically, the methods assume that Euler-Bernoulli beam theory is accurate enough to capture the behavior of the beam and furthermore, it is assumed that the properties of the beam are uniform along their span. Both static and dynamic measurement techniques are used [37].

1.2.1 Static Measurements of Stiffness

Figure 1.1 illustrates a simple approach to the measurement of the bending stiffness of beams. A concentrated mass m is attached to the tip of the cantilevered blade of length L and the deflection w due to the tip load is measured. The beam presenting uniform properties along its span is modeled using Euler-Bernoulli beam theory and its flap-wise bending stiffness, EI, is readily found from the following equations

$$\begin{aligned} \frac{d^2w}{dx^2} &= \frac{M}{EI}, \\ \frac{dw}{dx} &= \int_0^L \frac{-mg(L-x)}{EI} dx, \\ EI &= \frac{mgL}{2(dw/dx)}, \end{aligned} \tag{1.1}$$

where the last equation assumes the properties to be uniform along the beam's span.

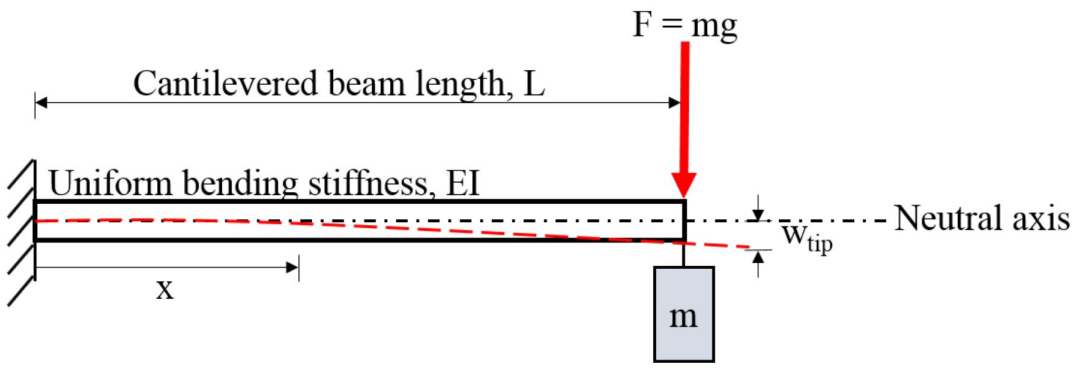

Figure 1.1: A blade modeled as an Euler-Bernoulli beam applied with a tip load [37].

A similar approach is used to measure the torsional stiffness of the beam. A tip torque, T, is applied at the tip of the beam and the resulting tip twist, ϕ, is measured as shown in fig. 1.2. The torsional stiffness, GJ, then follows from the following equations

$$\begin{aligned} \frac{d\phi}{dx} &= \frac{T}{GJ} \\ \phi &= \int_0^L \frac{T}{GJ} dx \\ GJ &= \frac{mgrL}{\phi} \end{aligned} \tag{1.2}$$

where the last equation assumes the properties to be uniform along the beam's span.

1.2.2 Dynamic Measurements of Stiffness

Dynamic measurements can also be used to measure stiffness properties. Typically, the natural vibration frequencies of the beam are measured, leading to an

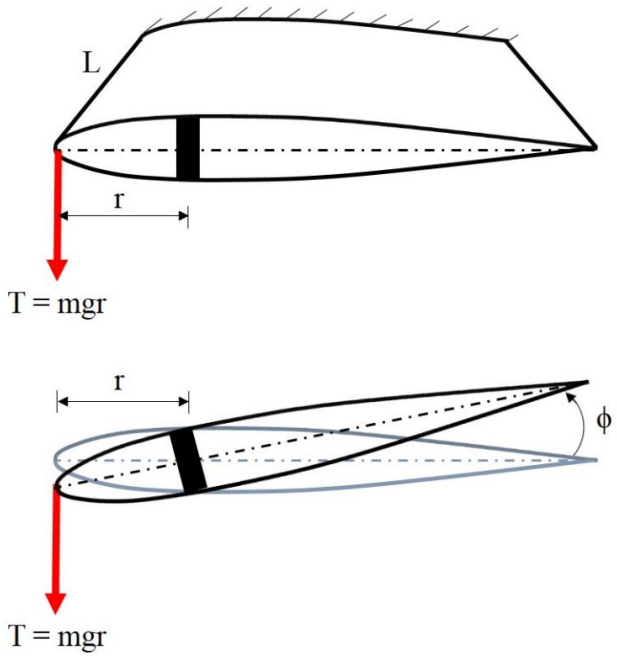

Figure 1.2: A blade modeled as an Euler-Bernoulli beam applied with a torque [37].

estimate of its stiffness. Figure 1.3 shows a typical test set-up: the same blade is hung vertically and an electro-mechanical shaker with a magnetic tip is used to apply a contact-free excitation force to the blade. The oscillations of the beam are recorded by a laser beam.

The approach requires the knowledge of the mass and mass moment of inertia of the beam per unit span, denoted, m and I_p, respectively. These quantities are measured easily. The following equations relate the sectional bending and torsional stiffnesses to the measured frequencies

$$\begin{aligned} EI &= 0.0809 m L^4 \omega_b^2 \\ GJ &= 2 I_p L^2 \omega_t^2, \end{aligned} \tag{1.3}$$

where ω_b and ω_t are the measured natural vibration frequency in bending and torsion, respectively.

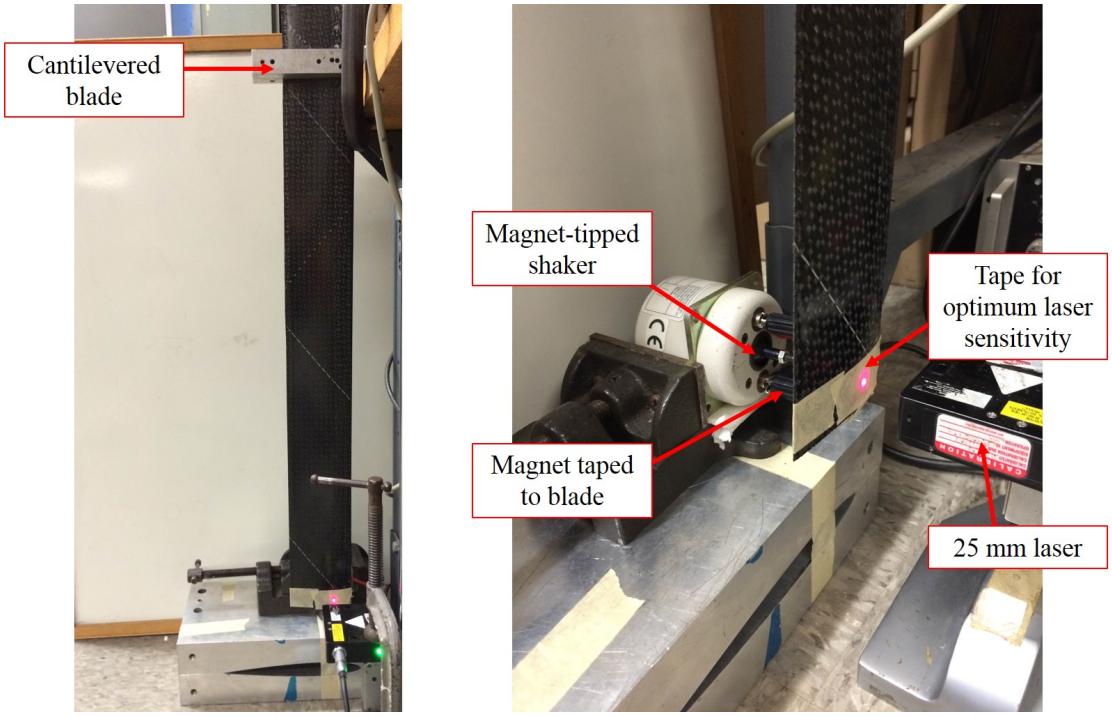

Figure 1.3: Frequency response test setup [37].

The simple measurement techniques presented in this section can be used to measure the sectional bending and torsional stiffness characteristics of beam presenting uniform properties along their span. These techniques, however, cannot be used to measure the complete six-by-six sectional stiffness matrix of the beam. Furthermore, these techniques are based on Euler-Bernoulli beam theory, which might not be accurate enough to capture the behavior of rotor blades made of heterogeneous, anisotropic materials.

1.3 Review of Strain Measurement Methodology

To develop more reliable and accurate experimental techniques for beam sectional stiffness evaluation, a detailed measurement of the strain field in the beam is

required. This section present a review of the various techniques used to measure strain field; the advantages and drawbacks of each approach will be highlighted. Both contacting and non-contacting measurements are reviewed.

1.3.1 Contacting Measurement Techniques

1.3.1.1 Strain gauge measurement techniques

Strain gauge measurement techniques have been evolving over the decades. Hoffmann [23] outlined the development of strain gauges techniques and provided an overview of their application. Traditional measurement methods, such as metal and semiconductor strain gauges, measure changes in electrical resistance. The former approach depends on the strain-resistivity relationship whereas the latter is based on the mobility of electron, as shown in figs. 1.4 and 1.5, respectively. For these devices, it is assumed that the strain gauge adheres to the tested article firmly and hence, the test article and the strain gauge undergo identical straining. In practice, the slightest debonding between the test article and the strain gauge causes systematic measurement errors. Strain gauge techniques provide a measurement of the strain at a point. To measure the complete strain field at the outer surface of a test article, a large number of gauges must be installed, a process that is both labor-intensive and error prone.

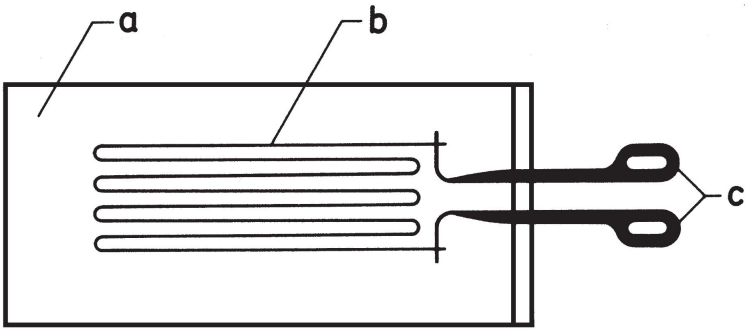

Figure 1.4: Simplified strain gauge. (a) Carrier material (b) Measuring grid (c) Connections

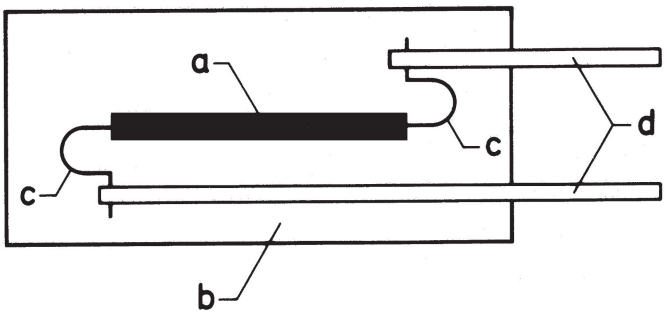

Figure 1.5: Simplified semiconductor gauge. (a) Measuring grid (b) Carrier material (c) Intermediate conductor (d) Connectiing Strips

1.3.1.2 Extensometer based measurement techniques

The word "extensometer" originates from "extension-meter:" these devices are used to measure extensional strain. In the contacting version of extensometers, the device is clipped to the test sample and measures the extension of the sample, as shown in fig 1.6. The physical contact between the specimen and the extensometer can potentially damage the specimen. Extensometers average the deformation over a finite distance: clearly, the measurement provides an average strain rather than the strain at a point.

Non-contacting extensometers have also been developed: a laser beam is pro-

jected onto the sample and its reflection is captured by a camera that infers changes in distance and hence, deformation. Figure 1.7 depicts a video extensometer, in which a digital camera takes a series of pictures of markers painted on the specimen and tracks their positions in time. The time history of the strain is then obtained via image processing. Using high-resolution digital cameras provides a versatile instrument able to measure strains in high-modulus and brittle materials or to track large deformations in ductile materials. Extensometers can achieve high accuracy but measure average strain distribution over a finite distance: high strain gradients cannot be investigated. Finally, it must be noted that extensometer cannot measure shear strains.

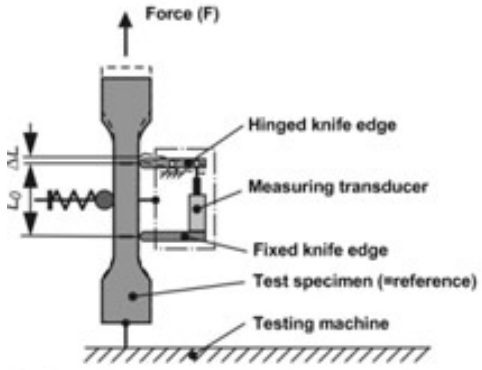

Figure 1.6: Schematic diagram of clip-on extensometer (https://knowledge.ulprospector.com/1420/pe-extensometer/).

1.3.1.3 Fiber optic sensors

Fiber optic sensors typically consist of a single optic fiber, or a network of optic fibers, embedded in the test article. As the test article deforms, the embedded optic fiber deforms, modifying the reflected wavelength of light travelling through

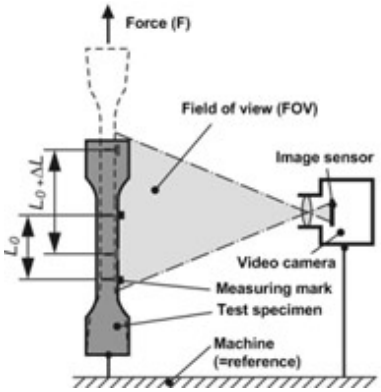

Figure 1.7: Schematic Diagram video extensometer (https://knowledge.ulprospector.com/1420/pe-extensometer/).

the fiber. Fiber optic sensors are light weight and provide high-resolution strain measurements. Rather than measuring the strain at a point, these sensors measure average deformation along the fiber; despite considerable effort, it is still not possible to measure sharp strain gradients with these devices. Of course, the optic fiber must be embedded in the test article during manufacturing, which might not be an easy task.

Table 1.1 lists the advantages and disadvantages of contacting measurement methods described in the previous paragraphs.

Table 1.1: Advantages and disadvantages of contacting measurements.

Technique	**Contacting strain measurement techniques**
Advantages	· Affordable · Able to measure internal strains · Usable in both rotating and non-rotating systems · Usable with obstructed view of the test article
Disadvantages	· Measure average strain only · Cannot measure high strain gradients · Setup procedure is complex and delicate · Can impact local mass/stiffness properties

The results listed in table 1.1 show that despite numerous desirable features, contacting strain measurements are not capable of producing measurement of the complete strain field at the external surface of a test article. In the next section, the attention turns to non-contacting techniques, which can be further categorized into interferometric and non-interferometric.

1.3.2 Non-contacting Measurement Techniques

1.3.2.1 Interferometric Measurements

Interferometric methods, reviewed by Hariharan [21], are based of interference of light waves: the Michaelson interferometer, depicted in fig. 1.8, is a prime example of this approach. The light beam projected from the source is split into two beams that travel different paths. The reflected beams coalesce at the splitter and are received by the detector. The interference of the two waves of identical frequency creates interference patterns due to their phase difference. Minute differences in the beam-traveled distance are detectable because visible light has a short wavelength. Because of its accuracy, interferometry is a reliable measurement approach.

Electronic speckle pattern interferometry (ESPI), also known as electronic holographic interferometry, is a well-known interferometric method. Figure 1.9 illustrates a typical ESPI setup. The hologram of the object and the reference beam are combined and projected on a television camera. Because of surface roughness, two beams of the same frequency interfere and produce the speckle pattern shown in fig 1.10. As the object deforms or moves, the distance to the camera changes,

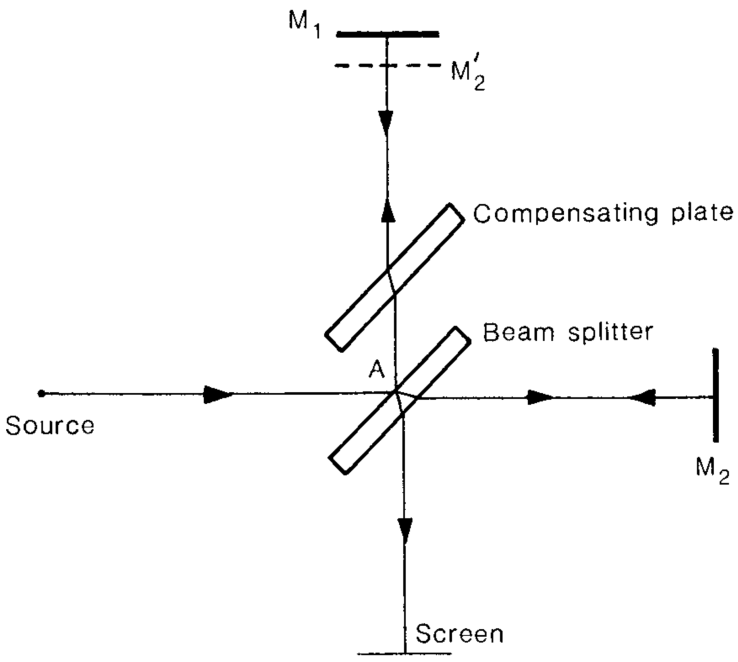

Figure 1.8: Michelson interferometer.

modifying the speckle pattern. Images are subtracted from each other to create the interference fringes shown in fig. 1.11. The camera is able to process the coarse speckle interferogram image for further evaluate the deformation. Although the coarse speckle results in coarse interference fringes, the resolution can be optimized by averaging multiple fringe patterns obtained from different speckle backgrounds.

Although EPSI presents high accuracy and can perform dynamic measurements, it cannot deal with rigid-body motions. Indeed rigid-body motion and deformation cannot be distinguished because a single fringe patter is analyzed. Furthermore, because the test article must be attached to the ESPI system, it is difficult to perform experiments on large structures such as full-scale rotor blades.

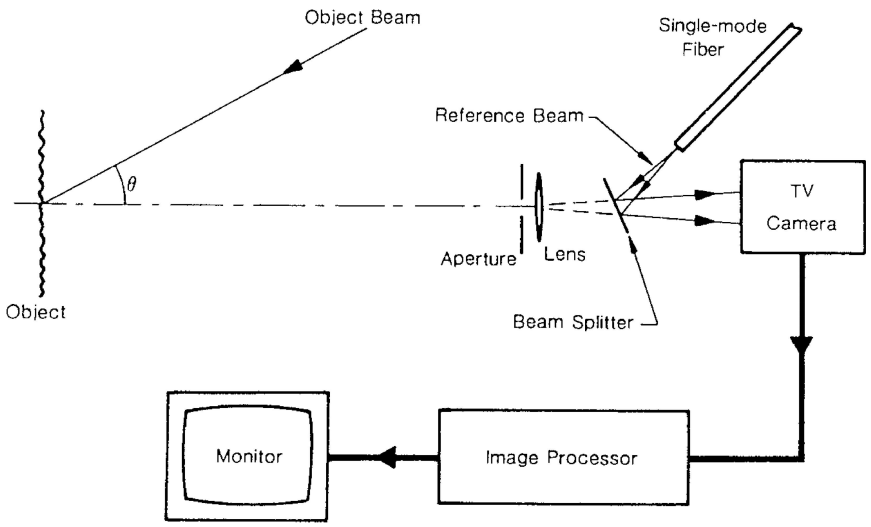

Figure 1.9: Typical electronic speckle pattern interferometer.

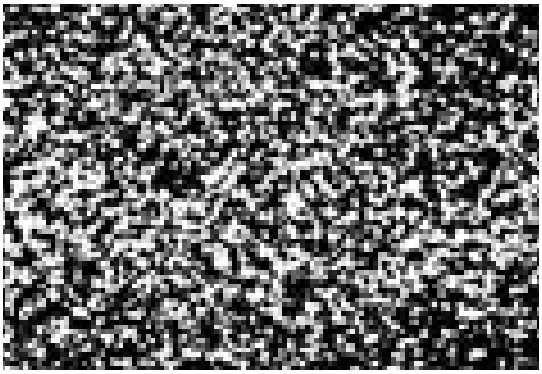

Figure 1.10: An example of speckle pattern.

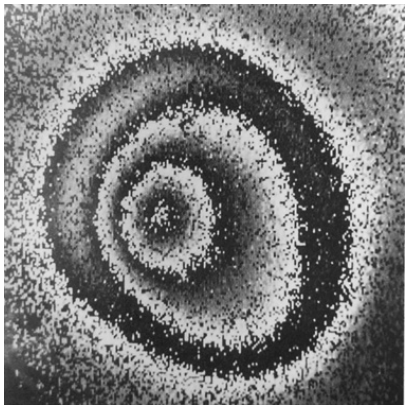

Figure 1.11: Example of fringes produced by ESPI (D. W. Robinson and D. C. Williams, *Opt.Commun.* 57, 2630, 1986).

1.3.2.2 Digital image correlation

Digital image correlation is a well-known, non-interferometric measurement system. It measures a full-field displacements and strains in both two and three dimensions under either static or dynamic conditions. The high-speed cameras and data acquisition system process the data efficiently. Additionally, because the cameras can be placed at any convenient distance from test article, all surface strain components can be measured, including shear strains. DIC is used easily on full-scale rotor structures.

1.4 Digital Image Correlation

"Digital image correlation" or DIC is composed of two high-resolution cameras and a software package; a VIC-3D DIC measurement system is shown in fig. 1.12. The principle of operation of DIC and its applications are well documented, see Sutton [35]. In general, DIC tracks movements of speckles or particles on digital images photographed by cameras and accordingly measures displacements in two or three dimensions.

As depicted in fig. 1.13, the cameras take pictures of an area on the surface of the test article, which is prepared with a random speckle pattern. The movements of these speckles are traced based on the images viewed by the cameras. Figure 1.14 shows a DIC measurement system. The data acquisition system evaluates the deformation by comparing pictures of the test article in its reference and deformed configurations and produces a full-field strain contour.

Figure 1.12: The VIC-3D DIC measurement system.

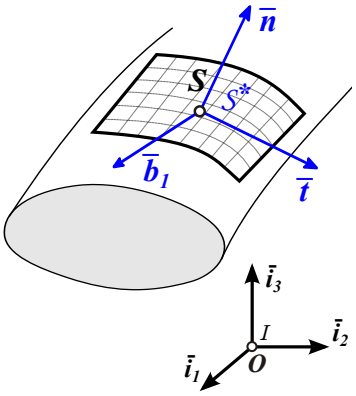

Figure 1.13: DIC evaluates a full-field strain on a specific area.

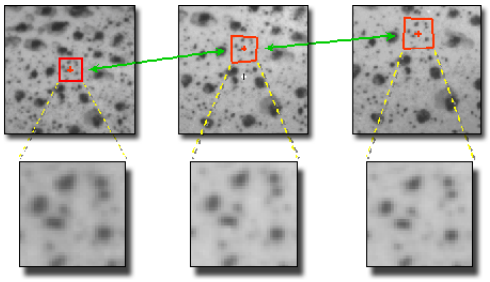

Figure 1.14: DIC measurement. (Correlated Solutions, Inc.)

DIC is able to measure structural deformation accurately in both two and three dimensions. Figure 1.15 shows how displacements can be evaluated and are highlighted in colored blocks.

Further image processing enables the computation of individual displacement

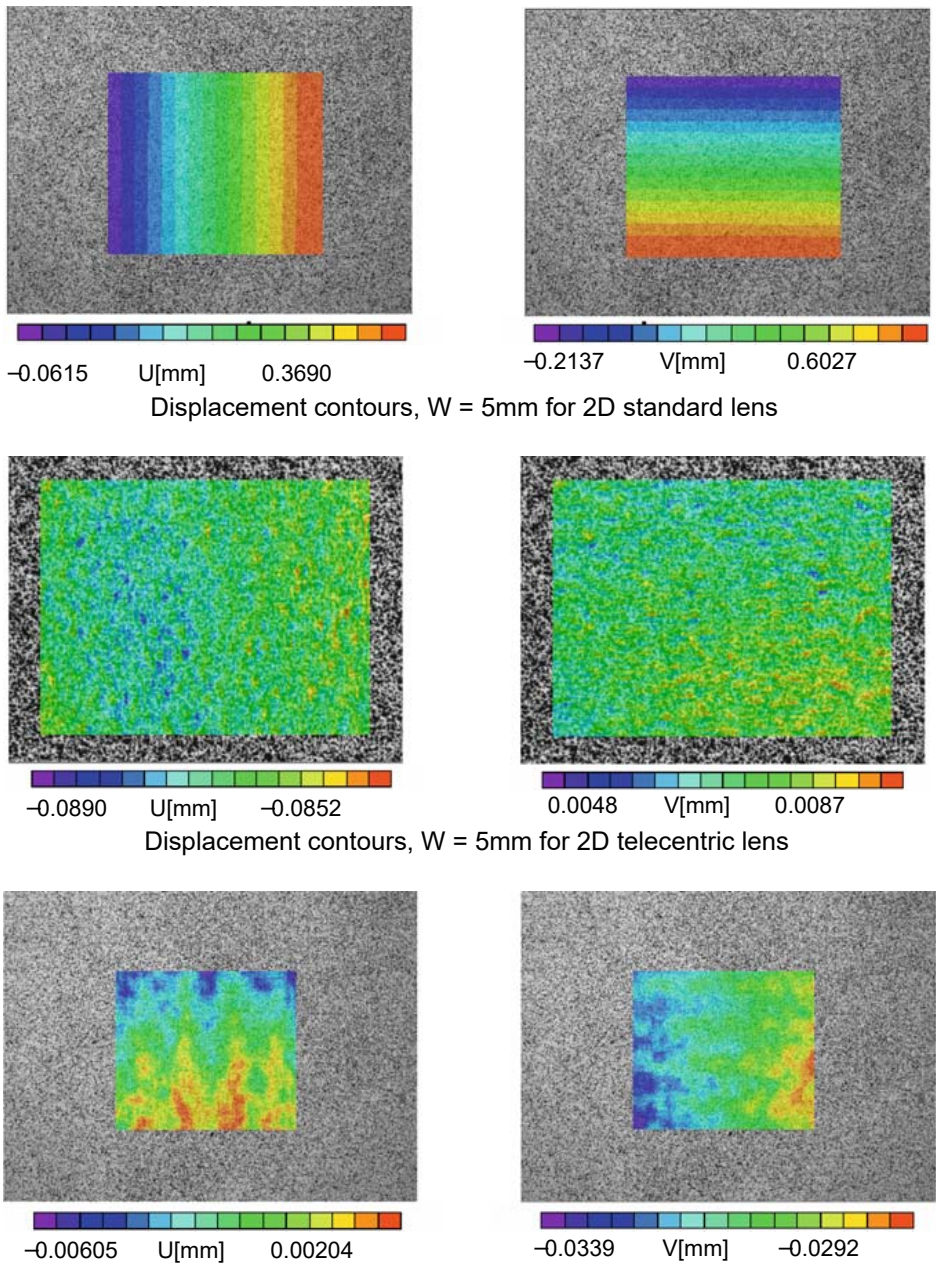

Figure 1.15: Reference results of horizontal and vertical displacement fields by VIC-2D for 2D images and out-of-plane displacement towards the camera by VIC-3D.

and strain components, as shown in fig 1.16.

Through a judicious use of interpolation, such as bilinear interpolation and Non-Uniform Rational B-Spline (NURBS) interpolation, DIC is able to process the

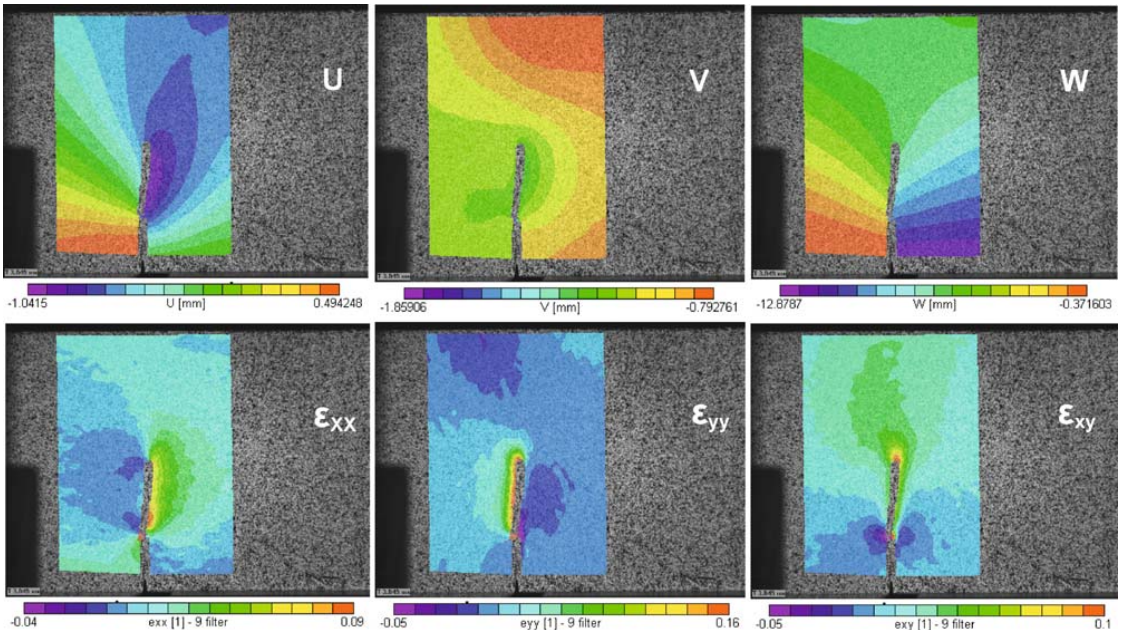

Figure 1.16: Reference results of displaying all displacements and in-plane strains.

discrete images to achieve sub-pixel level accuracy. Because it does not rely on interference fringes, DIC is capable of measuring both deformations and rigid-body motions. Although the resolution of the imaging system may limit the accuracy of measured strain and displacement fields, improved processing algorithm and high-resolution cameras can minimize these errors. Table 1.2 summarizes characteristics of interferometric and non-interferometric methods.

Table 1.2: Comparison of non-contacting measurements.

Non-contacting Strain Measurement	
Interferometric (ESPI)	· Speckle pattern generated by visible light/laser · Uses principle of optical interference · Resolution determined by the wavelength of light · Unable to distinguish between deformation and rigid-body motion
Non-interferometric (DIC)	· Random speckle pattern has to be generated manually · Analyzes digital images · Accuracy determined by the resolution of the cameras · Able to measure deformations and displacements simultaneously

Chapter 2: Review of SectionBuilder

SectionBuilder is a finite element based tool for the analysis of cross-sections of beams of arbitrary configuration made of anisotropic materials. It provides an exact solution of the 3D theory of elasticity under the following assumption: *(1)* strains and warping displacements are small; *(2)* cross-sectional geometry and material properties are arbitrary but uniform along the span; *(3)* the beam's span is much larger than the dimension of its cross-section. The first two assumptions imply that the beam can be analyzed using Saint Venant's beam theory [4], and the third one assumes the effects of extremity negligible. The foundation and principle of *SectionBuilder* are explained in the following sections.

2.1 Review of Three-dimensional Beam Theory

The term "Saint-Venant's problem" refers to a three-dimensional beam loaded at its end sections only. The investigation of Saint-Venant's problem provides the theoretical foundations for beam theory, a tool used widely in engineering applications. Saint-Venant considered prismatic bars made of isotropic materials whose sectional properties remain constant along their span; using a semi-inverse approach, he derived exact elasticity solutions for beams under torsion [10] and bending [11]. For

straight beams made of homogenous, isotropic materials, the three-dimensional elasticity equations reduce to two-dimensional Poisson's equations over the beam's cross-section [31,36]. Lekhnitskii [29] used the semi-inverse method to solve Saint-Venant's problem for beams made of homogeneous, anisotropic materials. For straight beams with specific cross-sectional shapes, analytical solutions of Saint-Venant's problem can be found.

For straight beams made of heterogenous materials, Iesan [24,25] developed a systematic approach to obtain the solutions of Saint-Venant's problem. He proved *(1)* that Saint-Venant's problem can be decomposed into extension-bending-torsion and flexure problems, *(2)* that the partial derivatives of the solutions of the extension-bending-torsion problem correspond to the beam's four rigid-body motions, and *(3)* that the partial derivatives of the solutions of the flexure problem are the solutions of extension-bending-torsion problem. Dong *et al.* [12, 27, 30] generalized Iesan's method using a semi-finite element discretization for the cross-section. In their work, warping displacements and sectional properties of the beam are found.

Berdichevsky [6] proposed the Variational Asymptotic Method (VAM), in which asymptotic analysis is applied to the energy functional. For beams, the ratio of a typical dimension of the cross-section to the beam's length is a small parameter used in the asymptotic expansion. In this approach, Saint-Venant's problem is reduced to a two-dimensional analysis over the beam's cross-section. A unified beam theory based on VAM was further refined by Atilgan *et al.* [1, 2], Hodges [22], and Yu *et al.* [39]. The variational asymptotic method can deal with beams with small initial curvatures. Buannic and Cartraud [8, 9] developed a two-scale asymptotic

expansion method for periodic heterogenous beam-like structures. Kim [26] generalized this approach to Saint-Venant's problem for straight, anisotropic beams. The dimensional reduction process is based on a formal asymptotic expansion, which splits the three-dimensional beam problem into two sets of recursive equations: a set of two-dimensional local recursive problems and a set of one-dimensional global recursive problems.

Giavotto *et al.* [17] presented a comprehensive solution strategy for Saint-Venant's problem. Their approach is based on a two-dimensional analysis of the beam's cross-section using finite elements and yields its stiffness characteristics in the form of a 6×6 sectional stiffness matrix. Furthermore, the three-dimensional strain field at any point of the cross-section can be recovered once the sectional strains are known. Their work also identifies the two types of solutions present in beams: the central solutions and the extremity solutions, as should be expected from Saint-Venant's principle. Borri *et al.* [7] generalized this methodology to naturally curved beams; the magnitudes of beam's initial curvatures are not required to be small in their approach.

Mielke [32, 33] found the center manifold of Saint-Venant's problem for a straight beam. He showed that this center manifold is a finite-dimensional manifold spanned by the twelve generalized eigenvectors associated with the null and purely imaginary eigenvalues. These twelve generalized eigenvectors form four Jordan chains; six of the eigenvectors correspond to the beam's rigid-body modes while the others six are the fundamental deformation modes of the beam (Saint-Venant's solution): extension, torsion, and bending and shearing in two directions.

Zhong [40] developed novel analytical techniques based on Hamilton's formalism. A Hamiltonian operator characterizes the stiffness of the structure and its null and purely imaginary eigenvalues give rise to the solution of Saint-Venant's problem. The eigenvalues with a non-vanishing real part give rise to decaying solutions and the associated characteristic decay length provide a quantification of Saint-Venant's principle. As previously stated by Mielke, Zhong also identified the Jordan chains associated with the eigenvalues of the Hamiltonian operator with a vanishing real part. Zhong [41] produced analytical solutions for planar elasticity problems and for three-dimensional straight beams made of isotropic and anisotropic materials, he outlined procedures for the determination of the twelve generalized eigenvectors.

Recently, a similar approach based on Hamilton's formalism was developed by Morandini *et al.* [34] who used numerical techniques to evaluate the Jordan form and associated generalized eigenvectors for straight beams made of both isotropic and anisotropic materials. Druz and Ustinov [14] also found the Jordan chain structure of Saint-Venant's problem for an elastic cylinder. They constructed Green's tensor for an elastic cylinder and expanded Green's tensor in terms of eigenvectors corresponding to the null eigenvalues. Druz *et al.* [13] further investigated the Saint-Venant's problem for naturally twisted beams. It was shown that elementary solutions of Saint-Venant's problem can be obtained from the solution of two types of boundary-value problems. A stiffness matrix relating the components of generalized forces and displacements was also obtained. Ustinov [38] generalized the approach to a cylinder with helical anisotropy.

Ladevèze and Simmonds [28] proposed a new approach for the analysis of

straight prismatic beams with piecewise constant cross-sections under arbitrary loading. They found that the complete solution can be divided into a long wavelength part, *i.e.,* the solution of Saint-Venant's problem, and a short wavelength, localized part, *i.e.,* extremity solutions due to discontinuity of sectional geometry and external loads. The solutions of Saint-Venant's problem were derived in terms of the sectional stress resultants, sectional displacements and rotations, and differential operators characterizing the cross-section geometry and material characteristics. Ladevèze and Simmonds' approach was expanded by El Fatmi and Zenzri [15, 16] with the aid of a semi-finite element discretization for cross-sections.

Bauchau and Han [5] developed an approach to the solution of Saint-Venant's problem based on Hamilton's formalism. The approach proceeds through a sequence of structure preserving transformations using symplectic matrices and decomposes the solution into its central and extremity components. The structure preserving transformations lead to a set of linear equations for the nodal warping and sectional compliance matrix; the explicit construction of the Jordan form is thereby avoided. The solutions of Saint-Venant's problem are found by projecting the governing equations onto the subspace associated with the Hamiltonian matrix's null and pure imaginary eigenvalues. The same authors [19] further generalized the approach to initially curved beams undergoing large motion but small strains.

The review presented in the previous paragraphs underlines a fundamental feature of Saint-Venant's problem: its solutions are the generalized eigenvectors associated with the null and purely imaginary eigenvalues of a Hamiltonian system. As shown by Zhong [41], many elasticity problems share this characteristic. Unfor-

tunately, the Hamiltonian matrix cannot be diagonalized; rather, it can be reduced to Jordan canonical form only. Furthermore, the Jordan form involves two chains, one of size four, the other of size two, both with a multiplicity of two. Finally, it will be shown in this paper that for helicoidal beams, the two chains of size four involve purely imaginary eigenvalues. These mathematical characteristic of the problem explain why its solution is so arduous: no reliable numerical procedure exists for the determination of the Jordan chains of matrices of large size and of the associated generalized eigenvectors. Indeed, the determination of generalized eigenvectors is known to be notoriously unstable, hampering the development of robust numerical procedures.

A novel solution strategy to Saint-Venant's problem for helicoidal beams is proposed, based on the construction of the subspace of the Hamiltonian matrix associated with its null and pure imaginary eigenvalues. Projection of the system's Hamiltonian onto this subspace reduces it to a Hamiltonian matrix of size 12×12. The explicit construction of the generalized eigenvectors associated with the null and pure imaginary eigenvalues is bypassed, enabling the computationally efficiency solution of large-scale, realistic problems. The following assumptions are made: *(1)* the beam's reference line is a helix; *(2)* cross-sectional geometry and material properties are arbitrary (heterogeneous and anisotropic), but remain uniform along the span; *(3)* strains and warping displacements remain small; *(4)* the beam's span is much larger than a characteristic dimension of its cross-section. The first assumption implies that the beam's reference line is of constant curvature. Due to the first three assumptions, the governing equations of the problem can be cast into a Hamiltonian

system with constant coefficients. The fourth assumption implies that the effects of the extremity solutions are negligible.

The analysis of beams featuring complex cross-sections and made anisotropic composite materials was first presented by Giavotto *et al.* [17]. Based on the Hamiltonian formalism, Bauchau and Han [5] have developed an exact solution of this problem in terms of the central and extremity solutions. The three-dimensional beam theory presented by Bauchau and Han [5, 19] forms the basis for the development of the viscoelastic models proposed in this paper. The central solution of the beam for linear elasticity is exact, while the extremity solution, at the edges of the beam, is negligible.

2.2 Kinematics of the Problem

Figure 2.1 depicts a naturally curved and twisted beam of length L, with a cross-section of arbitrary shape and area $\mathcal{A}$. The volume of the beam is generated by sliding the cross-section along the reference line of the beam, which is defined by an arbitrary curve in space denoted $\mathcal{C}$. Curvilinear coordinate α_1 defines the intrinsic parameterization of this curve, *i.e.*, it measures length along $\mathcal{C}$. Point $\mathbf{B}$ is located at the intersection of the reference line with the plane of the cross-section. The unit tangent

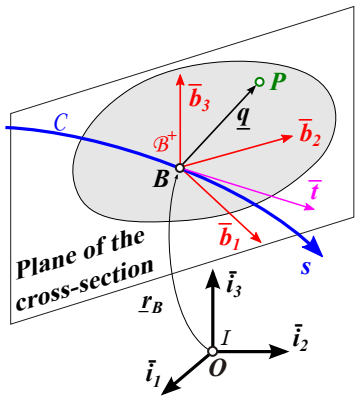

Figure 2.1: Configuration of a naturally curved beam.

vector to curve $\mathcal{C}$ is

$$\bar{t} = \frac{\partial \underline{r}_B}{\partial \alpha_1}, \tag{2.1}$$

where $\underline{r}_B$ is the position vector of point $\mathbf{B}$ with respect to the origin of the reference frame, $\mathcal{F} = [\mathbf{O}, \mathcal{I} = (\bar{\imath}_1, \bar{\imath}_2, \bar{\imath}_3)]$.

In the reference configuration, the cross-section is defined by frame $\mathcal{F}_c = \left[\mathbf{B}, \mathcal{B} = (\bar{b}_1, \bar{b}_2, \bar{b}_3)\right]$. The plane of the cross-section is determined by two mutually orthogonal unit vectors, $\bar{b}_2$ and $\bar{b}_3$; in general, the unit tangent vector, $\bar{t}$, to curve $\mathcal{C}$ is not aligned with unit vector $\bar{b}_1$, as illustrated in fig. 2.1. A set of material coordinates that naturally represent the configuration of the beam is selected as follows: α_1, α_2, and α_3, where the last two coordinates measure length along the directions of unit vectors $\bar{b}_2$ and $\bar{b}_3$, respectively.

The orientation of the sectional plane changes as it slides along curve $\mathcal{C}$. Consequently, basis $\mathcal{B}$ is a function of curvilinear variable α_1; the rotation tensor that brings basis $\mathcal{I}$ to basis $\mathcal{B}$ is denoted $\underline{\underline{R}}(\alpha_1)$. The following motion tensor [3] is defined

$$\underline{\underline{\mathcal{C}}}(\underline{r}_B, \underline{\underline{R}}) = \begin{bmatrix} \underline{\underline{R}} & \tilde{\underline{r}}_B \underline{\underline{R}} \\ \underline{\underline{0}} & \underline{\underline{R}} \end{bmatrix}. \tag{2.2}$$

The components of the beam's curvature vector in its initial configuration, resolved in basis $\mathcal{B}$, are then

$$\tilde{\mathcal{K}} = \underline{\underline{\mathcal{C}}}^{-1} \underline{\underline{\mathcal{C}}}', \tag{2.3}$$

where notation $(\cdot)'$ indicates a derivative with respect to $\bar{\alpha}_1$. It is verified easily that $\underline{\mathcal{K}}^T = \{\bar{t}^T, \underline{k}^T\}$, where $\underline{k} = \text{axial}(\underline{\underline{R}}^T \underline{\underline{R}}')$ is the curvature vector.

2.3 Strain Components

The derivation summarized here holds for beams undergoing large displacements and rotations, but strain components remain very small at all times. The components of the Green-Lagrange strain tensor are partitioned into the out-of-plane and in-plane strain components, denoted $\underline{\gamma}_O^T = \{\gamma_{11}, 2\gamma_{12}, 2\gamma_{13}\}$ and $\underline{\gamma}_I^T = \{\gamma_{22}, \gamma_{33}, 2\gamma_{23}\}$, respectively, defined as

$$\sqrt{g}\,\underline{\gamma}_O = \underline{\bar{u}}' + \underline{\underline{D}}_O\underline{\bar{u}}, \tag{2.4a}$$

$$\sqrt{g}\,\underline{\gamma}_I = \quad \underline{\underline{D}}_I\,\underline{\bar{u}}, \tag{2.4b}$$

where $\sqrt{g} = t_1 - k_3\alpha_2 + k_2\alpha_3$. The components of the strain tensor are collected into a single array,

$$\underline{\gamma} = \begin{Bmatrix} \underline{\gamma}_O \\ \underline{\gamma}_I \end{Bmatrix} = \underline{\underline{A}}\,\underline{u}' + \underline{\underline{B}}\,\underline{\bar{u}}. \tag{2.5}$$

In eqs. (2.4), the following differential operators were defined

$$\underline{\underline{D}}_O = \begin{bmatrix} d & -k_3 & k_2 \\ k_3 + \sqrt{g}\dfrac{\partial}{\partial\bar{\alpha}_2} & d & -k_1 \\ -k_2 + \sqrt{g}\dfrac{\partial}{\partial\alpha_3} & k_1 & d \end{bmatrix}, \quad \underline{\underline{D}}_I = \begin{bmatrix} 0 & \sqrt{g}\dfrac{\partial}{\partial\alpha_2} & 0 \\ 0 & 0 & \sqrt{g}\dfrac{\partial}{\partial\alpha_3} \\ 0 & \sqrt{g}\dfrac{\partial}{\partial\alpha_3} & \sqrt{g}\dfrac{\partial}{\partial\alpha_2} \end{bmatrix}, \tag{2.6}$$

where $d = -(t_2 - k_1\alpha_3)\partial(\cdot)/\partial\alpha_2 - (t_3 + k_1\alpha_2)\partial(\cdot)/\partial\alpha_3$. In eq. (2.5), the following differential operators were defined

$$\underline{\underline{A}} = \frac{1}{\sqrt{g}}\begin{bmatrix} \underline{\underline{I}} \\ \underline{\underline{0}} \end{bmatrix}, \quad \underline{\underline{B}} = \frac{1}{\sqrt{g}}\begin{bmatrix} \underline{\underline{D}}_O \\ \underline{\underline{D}}_I \end{bmatrix}. \tag{2.7}$$

2.4 Semi-discretization of the Displacement Field

Beam theory is characterized by one-dimensional, ordinary differential equations governing the displacement field assumed to be a function of the axial variable, α_1, only. In the above paragraphs, the displacement field has been treated as a general vector field depending on three independent variables, α_1, α_2, and α_3. To obtain a one-dimensional formulation, the following semi-discretization of the displacement field is performed,

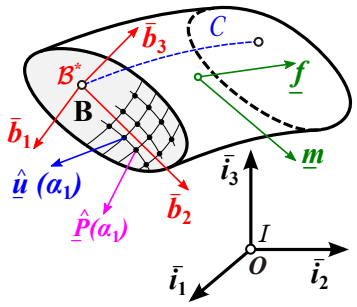

Figure 2.2: Semi-discretization of the beam. For clarity, the stresses are shown on one face of the differential element only.

$$\underline{u}(\alpha_1, \alpha_2, \alpha_3) = \underline{\underline{N}}(\alpha_2, \alpha_3)\hat{\underline{u}}(\alpha_1), \tag{2.8}$$

where matrix $\underline{\underline{N}}(\alpha_2, \alpha_3)$ stores the two-dimensional shape functions used in the discretization and array $\hat{\underline{u}}(\alpha_1)$ the nodal values of the non-dimensional displacement field. Notation $\hat{(\cdot)}$ indicates nodal quantities of the discretized model. This semi-discretization process is shown in fig 2.2 is a schematic manner: a typical cross-section of the beam is discretized using two-dimensional elements.

Let N be the number of nodes used to discretize the beam's cross-section and $n = 3N$ the total number of degrees of freedom. Introducing this discretization into

eq. (2.5) yields the components of the Green-Lagrange strain tensor as

$$\underline{\gamma} = \underline{\underline{A}}\,\underline{\underline{N}}\,\underline{\hat{u}}' + \underline{\underline{B}}\,\underline{\underline{N}}\,\underline{\hat{u}} = \underline{\underline{A}}_L\underline{\hat{u}}' + \underline{\underline{B}}_L\underline{\hat{u}} \tag{2.9}$$

Consider a rigid-body displacement field written as $\underline{u} = \underline{u}_R - \tilde{q}\underline{\phi}_R$, where $\underline{u}_R$ are the components of a rigid-body translation and $\underline{\phi}_R$ those of an infinitesimal rigid-body rotation. For convenience, the following non-dimensional motion array is defined $\underline{\mathcal{U}}_R^T = \{\underline{u}_R^T, \underline{\phi}_R^T\}$ and at a specific point of the cross-section, components of the rigid-body motion resolved in the material basis become

$$\begin{Bmatrix} u_1 \\ u_2 \\ u_3 \end{Bmatrix} = \underline{u}_R - \tilde{q}\underline{\phi}_R = \begin{bmatrix} 1 & 0 & 0 & 0 & \alpha_3 & -\alpha_2 \\ 0 & 1 & 0 & -\alpha_3 & 0 & 0 \\ 0 & 0 & 1 & \bar{\alpha}_2 & 0 & 0 \end{bmatrix} \begin{Bmatrix} \underline{u}_R \\ \underline{\phi}_R \end{Bmatrix} = \underline{\underline{z}}\,\underline{\mathcal{U}}_R = \underline{\underline{N}}\,\underline{\underline{Z}}\,\underline{\mathcal{U}}_R, \tag{2.10}$$

where $\underline{\mathcal{U}}_R = \underline{\underline{\mathcal{C}}}^{-1}\underline{\mathcal{U}}_R$ and matrix $\underline{\underline{Z}}$ stacks the rows of matrix $\underline{\underline{z}}$ for each of the nodes of the model.

2.5 The Central Solution

The central solution is an exact solution of the linear theory of three-dimensional elasticity for beams presenting uniform geometric and material characteristics along their span and is valid far away from the beam's edges, where all extremity solutions become negligible. The kinematic assumptions underpinning commonly used beam theories are eliminated altogether and yet, exact solutions are obtained for the central behavior of the beam. The accuracy of the solution is limited by the discretization inherent to the finite element method only.

An important feature of the central solution is that it provides the three-dimensional strain state at any point of the cross-section given the stress resultants at that spanwise location [5,19,20]. The stress resultants, denoted $\underline{\mathcal{F}}^T = \{\underline{F}^T, \underline{M}^T\}$, involve the three sectional forces, $\underline{F}$, consisting of the axial force and two transverse shear forces, and the sectional moments, $\underline{M}$, consisting of the twisting moment and two bending moments, all resolved in basis $\mathcal{B}$. The three-dimensional strain components at any point of the beam, denoted $\underline{\gamma}(\alpha_1, \alpha_2, \alpha_3)$, are proportional to the sectional forces,

$$\underline{\gamma}(\alpha_1, \alpha_2, \alpha_3) = \left[\underline{\underline{A}}_L(\underline{\underline{Z}}\,\underline{\underline{\mathcal{S}}} + \underline{\underline{W}}\tilde{\mathcal{K}}^T) + \underline{\underline{B}}_L\underline{\underline{W}}\right]\underline{\mathcal{F}}(\alpha_1), \tag{2.11}$$

where matrix $\underline{\underline{W}}(\alpha_2, \alpha_3)$ stores the nodal warping field; the columns of this matrix represent the warping induced by unit sectional stress resultants. Symmetric matrix $\underline{\underline{\mathcal{S}}}$ is the sectional compliance matrix for the central solution, *i.e.*,

$$\underline{\mathcal{E}} = \underline{\underline{\mathcal{S}}}\,\underline{\mathcal{F}}, \tag{2.12}$$

where array $\underline{\mathcal{E}}$ stores the sectional strains consisting of the axial strain and two transverse shear strains, and the sectional curvatures consisting of the twist rate and two bending curvatures, all resolved in basis $\mathcal{B}$.

Equation (2.11) implies that the complete three-dimensional strain field at any point of the cross-section can be expressed in terms of the six sectional stress resultants only. A detailed derivation of the central solution is found in Bauchau

and Han [5, 19].

As was done for the components of the Green-Lagrange strain tensor in eq. (2.4), the components of the convected Cauchy stress tensor are split into their out-of- and in-plane components, denoted $\underline{\tau}_O^T = \{\tau_{11}, \tau_{12}, \tau_{13}\}$ and $\underline{\tau}_I^T = \{\tau_{22}, \tau_{33}, \tau_{23}\}$, respectively. The array of convected Cauchy stress components then becomes $\underline{\tau}^T = \{\underline{\tau}_O^T, \underline{\tau}_I^T\}$ and the material constitutive laws are stated as

$$\underline{\tau} = \underline{\underline{\mathcal{D}}}\,\underline{\gamma}, \tag{2.13}$$

where matrix $\underline{\underline{\mathcal{D}}}$, of size 6×6, stores the components of material stiffness tensor resolved the material basis.

Chapter 3: Proposed approach for the measurement of sectional stiffnesses

The proposed approach for the measurement of the sectional stiffness properties of beams can be described as follows. The beam is subjected to a known set of loads and the six sectional loads at a span-wise location, three forces and three moments, are measured. Because the desired six-by-six sectional stiffness matrix relates the six sectional loads to the six sectional deformation measures, an independent measurement of the six sectional deformation measures is required to evaluate the sectional stiffness matrix. In the proposed approach, the six sectional deformation measures will be extracted from the full strain field measurement obtained from DIC.

The critical part of the proposed measurement approach is to relate the six sectional deformation measures at a span-wise location, three sectional strains and three sectional curvatures, to the DIC measured strain field at the outer surface of the beam. This topic is analyzed in details in this chapter. Figure 3.1 depict this key issue in a conceptual manner. The left-hand side of the figure shows the strain field over the outer surface of a beam as calculated by *SectionBuilder*. The right-hand side of the figure shows the strain field over the outer surface of a beam

as measured by DIC.

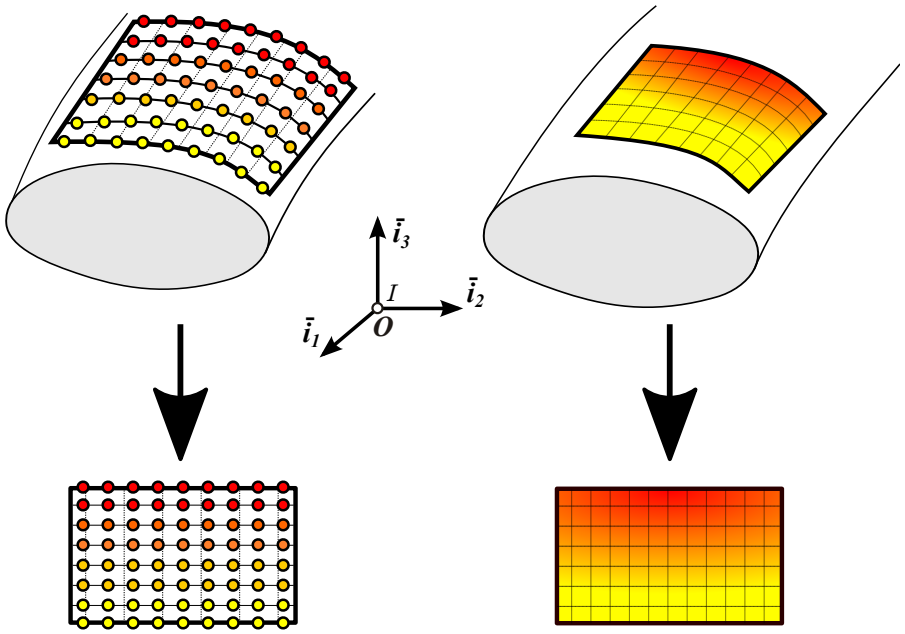

Figure 3.1: Simulation for *SectionBuilder*-predicted and DIC-viewed strains.

The strain at any point the outer surface of the beam can be evaluated in *SectionBuilder* using eq. (2.11). Furthermore, the strain field depends on the six sectional deformation measures only. By matching the strain fields predicted by *SectionBuilder* and measured by DIC, it is possible to evaluate the six sectional deformation measures. Details of this procedure are presented below.

3.1 Computed and measured strain fields

DIC measures the two-dimensional strains field over the outer surface of the beam that is subjected to various loading conditions. A *SectionBuilder* model of the beam's cross-section subjected to the same loading conditions predicts the two-dimensional strains field over the outer surface of the same beam. To compare these

two strain fields, two condition are required: *(1)* the strains must be computed at the same points, denoted "sensor points," over the outer surface of the beam and *(2)* the strain components must be resolved in the same coordinate system.

Figure 3.2 shows a number of sensor points at a specific span-wise location on the outer surface of the beam. These strain components are collected in array $\underline{\varepsilon}_i^{(j)}$, where subscript $(\cdot)_i$, $i = 1, 2, \ldots, N$, indicates the location of the sensor point and superscript $(\cdot)^{(j)}$, where $j = 1, 2, \ldots, L$, indicates the loading condition.

The strain components at different sensor points for loading case (j) are collected into array $\underline{\epsilon}^{(j)}$, of size $6N$. Furthermore, all the strain components at all sensor point locations for all loading conditions are collected into array $\underline{\mathcal{E}}$, of size $6NL$. An explicit definition of these array is

$$\underline{\epsilon}_{(6N)}^{(j)} = \begin{Bmatrix} \underline{\varepsilon}_1^{(j)} \\ \underline{\varepsilon}_2^{(j)} \\ \vdots \\ \underline{\varepsilon}_N^{(j)} \end{Bmatrix}, \quad \underline{\mathcal{E}}_{(6NL)} = \begin{Bmatrix} \underline{\epsilon}^{(1)} \\ \underline{\epsilon}^{(2)} \\ \vdots \\ \underline{\epsilon}^{(L)} \end{Bmatrix}. \tag{3.1}$$

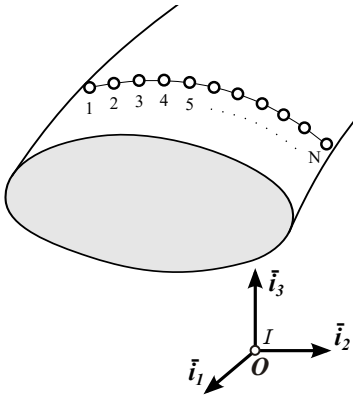

Figure 3.2: Installing N sensors on the desired surface.

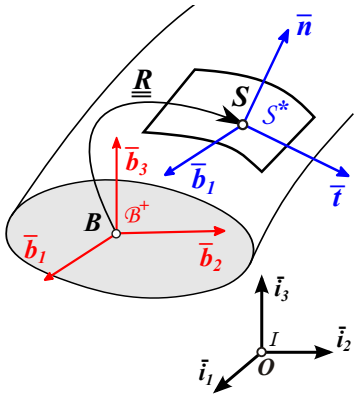

Figure 3.3: Rotation from basis $\mathcal{B}$ to basis $\mathcal{S}$.

3.2 Rotating the Strain Components

As discussed in section 1.4, the DIC cameras only measure the strain components on the outer surface of the beam. These strain components are resolved in the local coordinate system, $\mathcal{F}_s = \left[\mathbf{S}, \mathcal{S} = (\bar{b}_1, \bar{t}, \bar{n})\right]$, defined in fig 3.3, where unit vectors $\bar{t}$ and $\bar{n}$ are tangential and normal to the outer surface of the beam, respectively. To compare these strain components with those computed by *SectionBuilder*, they must be rotated to the cross-sectional coordinate system, $\mathcal{F}_c = \left[\mathbf{B}, \mathcal{B} = (\bar{b}_1, \bar{b}_2, \bar{b}_3)\right]$, also defined in fig 3.3. Unit vector $\bar{b}_1$ is normal to the place of the cross-section and unit vectors $\bar{b}_2$ and $\bar{b}_3$ define the plane of the cross-section.

The rotation tensor [3] that brings basis $\mathbf{B}$ to basis $\mathbf{S}$ is

$$\underline{\underline{R}} = \begin{bmatrix} 1 & 0 & 0 \\ 0 & C_\alpha & -S_\alpha \\ 0 & S_\alpha & C_\alpha \end{bmatrix}, \tag{3.2}$$

where the angle between unit vectors $\bar{b}_2$ and $\bar{t}$ is denoted α, $S_\alpha = \sin\alpha$ and $C_\alpha = \cos\alpha$.

The strain components measure by the DIC process are collected in array $\underline{\varepsilon}^*$,

$$\underline{\varepsilon}^* = \begin{Bmatrix} \varepsilon^*_{11} \\ \varepsilon^*_{tt} \\ \gamma^*_{1t} \end{Bmatrix} = \begin{Bmatrix} \varepsilon^*_{11} \\ \varepsilon^*_{tt} \\ 2\varepsilon^*_{1t} \end{Bmatrix}, \tag{3.3}$$

where superscript $(\cdot)^*$ indicates the strain components resolved in basis $\mathcal{S}$, and notation $(\cdot)_t$ indicates the tangential direction to the surface. Notation γ and ε indicates the engineering strain components and the tensor strain components, respectively, $\gamma = 2\,\varepsilon$. With this notation at hand, the complete strain tensor becomes

$$\underline{\varepsilon}^* = \begin{bmatrix} \varepsilon^*_{11} & \varepsilon^*_{1t} & \varepsilon^*_{1n} \\ \varepsilon^*_{1t} & \varepsilon^*_{tt} & \varepsilon^*_{tn} \\ \varepsilon^*_{1n} & \varepsilon^*_{tn} & \varepsilon^*_{nn} \end{bmatrix}. \tag{3.4}$$

Note that strain components ε^*_{nn}, ε^*_{1n}, and ε^*_{tn}, where the subscription $(\cdot)_n$ indicates normal direction to the surface, are not measured by the DIC process.

The strain components resolved in sectional basis $\mathcal{B}$, denoted $\underline{\varepsilon}^+$, are found using the rules of transformation for the components of second order tensors [4]

$$\begin{aligned}\underline{\varepsilon}^+ = \underline{\underline{R}}\,\underline{\varepsilon}^*\,\underline{\underline{R}}^T &= \begin{bmatrix} \varepsilon^+_{11} & \varepsilon^+_{12} & \varepsilon^+_{13} \\ \varepsilon^+_{12} & \varepsilon^+_{22} & \varepsilon^+_{23} \\ \varepsilon^+_{13} & \varepsilon^+_{23} & \varepsilon^+_{33} \end{bmatrix} \\ &= \begin{bmatrix} \varepsilon^*_{11} & \varepsilon^*_{1t}C_\alpha - \varepsilon^*_{1n}S_\alpha & \varepsilon^*_{1n}C_\alpha + \varepsilon^*_{1t}S_\alpha \\ \varepsilon^*_{1t}C_\alpha - \varepsilon^*_{1n}S_\alpha & \varepsilon^*_{tt}C^2_\alpha + \varepsilon^*_{nn}S^2_\alpha - \varepsilon^*_{tn}S_{2\alpha} & (\varepsilon^*_{tt} - \varepsilon_{nn})S_\alpha C_\alpha + \varepsilon^*_{tn}C_{2\alpha} \\ \varepsilon^*_{1n}C_\alpha + \varepsilon^*_{1t}S_\alpha & (\varepsilon^*_{tt} - \varepsilon^*_{nn})S_\alpha C_\alpha + \varepsilon^*_{tn}C_{2\alpha} & \varepsilon^*_{tt}S^2_\alpha + \varepsilon^*_{nn}C^2_\alpha + \varepsilon^*_{tn}S_{2\alpha} \end{bmatrix}. \end{aligned} \tag{3.5}$$

3.3 Local Equilibrium Conditions

While transformation of strain component equation (3.5) is correct, it involves strain components that were not measured by the DIC process. Consequently, additional information is need to perform the rotation. This additional information comes from the local equilibrium conditions that must be satisfied to the outer surface of the beam: Newton's laws implies the vanishing of the stress component normal to the surface and of the two shear stress components acting in this plane. These three additional conditions will be used to evaluate the strain components that were not measured directly by the DIC process.

To express these conditions, the rules of transformation for the components of second order tensors [4] are now applied to the components of the stress tensor to

find

$$\underline{\underline{R}}^T \underline{\underline{\tau}}^+ \underline{\underline{R}} = \underline{\underline{\tau}}^*, \tag{3.6}$$

where notation $\underline{\underline{\tau}}^+$ and $\underline{\underline{\tau}}^*$ indicates that stresses components resolved in bases $\mathcal{B}$ and $\mathcal{S}$, respectively.

As was done in section 2.5, the stress array, $\underline{\tau}^*$, is partitioned as $\underline{\tau}^{*T} = \{\underline{\tau}_O^{*T}, \underline{\tau}_I^{*T}\}$, where the out-of-plane components are $\underline{\tau}_O^{*T} = \{\tau_{11}^*, \tau_{1t}^*, \tau_{1n}^*\}$ and the in-plane components are $\underline{\tau}_I^{*T} = \{\tau_{tt}^*, \tau_{nn}^*, \tau_{tn}^*\}$. The stress-strain relationships, see eq. (2.13), now become

$$\underline{\tau}^* = \begin{bmatrix} \underline{\tau}_O^* \\ \underline{\tau}_I^* \end{bmatrix} = \underline{\underline{\mathcal{D}}}^* \begin{bmatrix} \underline{\gamma}_O^* \\ \underline{\gamma}_I^* \end{bmatrix}, \tag{3.7}$$

where the out-of-plane components are $\underline{\gamma}_O^{*T} = \{\gamma_{11}^*, 2\gamma_{1t}^*, 2\gamma_{1n}^*\}$ and the in-plane components are $\underline{\gamma}_I^{*T} = \{\gamma_{tt}^*, \gamma_{nn}^*, 2\gamma_{tn}^*\}$.

An alternative partitioning of eq. (3.7) is written in terms of the strain components measured by the DIC process, indicated by subscript $(\cdot)_{mm}$, and those that are not, indicated by subscript $(\cdot)_{nm}$, leading to

$$\begin{bmatrix} \underline{\tau}_{mm}^* \\ \underline{\tau}_{nm}^* \end{bmatrix} = \left[\begin{array}{c|c} \underline{\underline{\mathcal{D}}}_{mm}^* & \underline{\underline{\mathcal{D}}}_{nm}^* \\ \hline \underline{\underline{\mathcal{D}}}_{nm}^{*T} & \underline{\underline{\mathcal{D}}}_{nn}^* \end{array}\right] \begin{bmatrix} \underline{\varepsilon}_{mm}^* \\ \underline{\varepsilon}_{nm}^* \end{bmatrix}, \tag{3.8}$$

where $\underline{\tau}_{mm}^{*T} = \{\tau_{11}^*, \tau_{tt}^*, \tau_{1t}^*\}$, $\underline{\tau}_{nm}^{*T} = \{\tau_{nn}^*, \tau_{1n}^*, \tau_{tn}^*\}$, $\underline{\varepsilon}_{mm}^{*T} = \{\varepsilon_{11}^*, \varepsilon_{tt}^*, 2\gamma_{1t}^*\}$, and $\underline{\varepsilon}_{nm}^{*T} = \{\varepsilon_{nn}^*, 2\gamma_{1n}^*, 2\gamma_{tn}^*\}$.

With this notation at hand, the local equilibrium equations imply $\underline{\tau}_{nm}^* = \underline{0}$, leading to

$$\underline{\tau}_{nm}^* = \underline{\underline{\mathcal{D}}}_{nm}^{*T} \underline{\varepsilon}_{mm}^* + \underline{\underline{\mathcal{D}}}_{nn}^* \underline{\varepsilon}_{nm}^* = \underline{0}. \tag{3.9}$$

The strains components that were not measured by the DIC process now result as

$$\underline{\varepsilon}^*_{nm} = -\underline{\underline{\mathcal{D}}}^{*-1}_{nn}\,\underline{\underline{\mathcal{D}}}^{*T}_{nm}\,\underline{\varepsilon}^*_{mm}. \tag{3.10}$$

Finally, the complete strain array is found to be

$$\begin{bmatrix}\underline{\varepsilon}^*_{mm}\\ \underline{\varepsilon}^*_{nm}\end{bmatrix} = \begin{bmatrix}\underline{\underline{I}}\\ -\underline{\underline{\mathcal{D}}}^{*\,-1}_{nn}\,\underline{\underline{\mathcal{D}}}^{*T}_{nm}\end{bmatrix}\underline{\varepsilon}^*_{mm}. \tag{3.11}$$

3.4 Three-dimensional Solutions

With the notation introduced in this chapter, the recovery relationships for the central solution, see eq. (2.11) can be recast as

$$\underline{\varepsilon}^+_{\mathrm{SB}} = \left[\underline{\underline{A}}_L(\underline{\underline{Z}}\,\underline{\underline{\mathcal{S}}} + \underline{\underline{W}}\tilde{\mathcal{K}}^T) + \underline{\underline{B}}_L\underline{\underline{W}}\right]\underline{\mathcal{F}}. \tag{3.12}$$

On the other hand, the strain components measured by the DIC process and rotated to the sectional basis, see eq. (3.5), are

$$\underline{\varepsilon}^+_{\mathrm{DIC}} = \begin{Bmatrix}\underline{\varepsilon}^+_O\\ \underline{\varepsilon}^+_I\end{Bmatrix} = \left\{\begin{array}{c}\varepsilon^+_{11}\\ \varepsilon^+_{1t}C_\alpha - \varepsilon^+_{1n}S_\alpha\\ \varepsilon^+_{1n}C_\alpha + \varepsilon^+_{1t}S_\alpha\\ \hline \varepsilon^+_{tt}C^2_\alpha + \varepsilon^+_{nn}S^2_\alpha - \varepsilon^+_{tn}S_{2\alpha}\\ \varepsilon^+_{tt}S^2_\alpha + \varepsilon^+_{nn}C^2_\alpha + \varepsilon^+_{tn}S_{2\alpha}\\ (\varepsilon^+_{tt} - \varepsilon^+_{nn})S_\alpha C_\alpha + \varepsilon^+_{tn}C_{2\alpha}\end{array}\right\}. \tag{3.13}$$

The proposed approach imposes the condition that $\underline{\varepsilon}^+_{\mathrm{SB}} = \underline{\varepsilon}^+_{\mathrm{DIC}}$ at all sensor point locations and for all loading conditions. The unknowns of the problem are the 21 components of the sectional compliance matrix appearing in eq. (3.12). Be-

cause this set of linear equations is highly redundant, an appropriate data reduction procedure must be developed and is presented in the next section.

3.5 Data Reduction Process

The recovery relationships, see eq. (3.12), applied to the sensor point at location 1, imply

$$\begin{aligned}\underline{\varepsilon}_1^{(j)} &= \left[\underline{\underline{A}}_L(\underline{\underline{Z}}\,\underline{\underline{\mathcal{S}}} + \underline{\underline{W}}\tilde{\mathcal{K}}^T) + \underline{\underline{B}}_L\underline{\underline{W}}\right]_1 \underline{\mathcal{F}}^{(j)} \\ &= \underline{\underline{A}}_{L1}\underline{\underline{Z}}_1\,\underline{\underline{\mathcal{S}}}\,\underline{\mathcal{F}}^{(j)} + (\underline{\underline{A}}_{L1}\underline{\underline{W}}_1\tilde{\mathcal{K}}^T + \underline{\underline{B}}_{L1}\underline{\underline{W}}_1)\underline{\mathcal{F}}^{(j)} \\ &= \underline{\underline{U}}_1\underline{\underline{\mathcal{S}}}\,\underline{\mathcal{F}}^{(j)} + \underline{\underline{V}}_1\underline{\mathcal{F}}^{(j)},\end{aligned} \tag{3.14}$$

where the following matrices were defined

$$\underline{\underline{U}}_1 = \underline{\underline{A}}_{L1}\underline{\underline{Z}}_1, \tag{3.15a}$$

$$\underline{\underline{V}}_1 = \underline{\underline{A}}_{L1}\underline{\underline{W}}_1\tilde{\mathcal{K}}^T + \underline{\underline{B}}_{L1}\underline{\underline{W}}_1. \tag{3.15b}$$

Next, term $\underline{\underline{\mathcal{S}}}\,\underline{\mathcal{F}}^{(j)}$ in eq. (3.14) is recast as follows

$$
\begin{aligned}
\underline{\underline{\mathcal{S}}}\,\underline{\mathcal{F}}^{(j)} &= \underbrace{\begin{bmatrix} S_{11} & S_{12} & S_{13} & S_{14} & S_{15} & S_{16} \\ S_{12} & S_{22} & S_{23} & S_{24} & S_{25} & S_{26} \\ S_{13} & S_{23} & S_{33} & S_{34} & S_{35} & S_{36} \\ S_{14} & S_{24} & S_{34} & S_{44} & S_{45} & S_{46} \\ S_{15} & S_{25} & S_{35} & S_{45} & S_{55} & S_{56} \\ S_{16} & S_{26} & S_{36} & S_{46} & S_{56} & S_{66} \end{bmatrix}}_{6\times 6} \underbrace{\begin{Bmatrix} F_1^{(j)} \\ F_2^{(j)} \\ F_3^{(j)} \\ F_4^{(j)} \\ F_5^{(j)} \\ F_6^{(j)} \end{Bmatrix}}_{6\times 1} \\
&= \underbrace{\left[\begin{array}{c|c|c|c|c|c} \underline{\underline{\mathbb{F}}}_1^{(j)} & \underline{\underline{\mathbb{F}}}_2^{(j)} & \underline{\underline{\mathbb{F}}}_3^{(j)} & \underline{\underline{\mathbb{F}}}_4^{(j)} & \underline{\underline{\mathbb{F}}}_5^{(j)} & \underline{\underline{\mathbb{F}}}_6^{(j)} \end{array}\right]}_{6\times 21} \underbrace{\left\{\begin{array}{c} S_{11} \\ S_{12} \\ S_{13} \\ S_{14} \\ S_{15} \\ S_{16} \\ \hline S_{22} \\ S_{23} \\ S_{24} \\ S_{25} \\ S_{26} \\ \hline S_{33} \\ S_{34} \\ S_{35} \\ S_{36} \\ \hline S_{44} \\ S_{45} \\ S_{46} \\ \hline S_{55} \\ S_{56} \\ \hline S_{66} \end{array}\right\}}_{21\times 1} \\
&= \underline{\underline{G}}^{(j)}\underline{S},
\end{aligned}
\tag{3.16}
$$

where the following matrices were defined

$$\underline{\underline{\mathbb{F}}}_1^{(j)} = \begin{bmatrix} F_1^{(j)} & F_2^{(j)} & F_3^{(j)} & F_4^{(j)} & F_5^{(j)} & F_6^{(j)} \\ 0 & F_1^{(j)} & 0 & 0 & 0 & 0 \\ 0 & 0 & F_1^{(j)} & 0 & 0 & 0 \\ 0 & 0 & 0 & F_1^{(j)} & 0 & 0 \\ 0 & 0 & 0 & 0 & F_1^{(j)} & 0 \\ 0 & 0 & 0 & 0 & 0 & F_1^{(j)} \end{bmatrix}, \underline{\underline{\mathbb{F}}}_2^{(j)} = \begin{bmatrix} 0 & 0 & 0 & 0 & 0 \\ F_2^{(j)} & F_3^{(j)} & F_4^{(j)} & F_5^{(j)} & F_6^{(j)} \\ 0 & F_2^{(j)} & 0 & 0 & 0 \\ 0 & 0 & F_2^{(j)} & 0 & 0 \\ 0 & 0 & 0 & F_2^{(j)} & 0 \\ 0 & 0 & 0 & 0 & F_2^{(j)} \end{bmatrix},$$

$$\underline{\underline{\mathbb{F}}}_3^{(j)} = \begin{bmatrix} 0 & 0 & 0 & 0 \\ 0 & 0 & 0 & 0 \\ F_3^{(j)} & F_4^{(j)} & F_5^{(j)} & F_6^{(j)} \\ 0 & F_3^{(j)} & 0 & 0 \\ 0 & 0 & F_3^{(j)} & 0 \\ 0 & 0 & 0 & F_3^{(j)} \end{bmatrix}, \underline{\underline{\mathbb{F}}}_4^{(j)} = \begin{bmatrix} 0 & 0 & 0 \\ 0 & 0 & 0 \\ 0 & 0 & 0 \\ F_4^{(j)} & F_5^{(j)} & F_6^{(j)} \\ 0 & F_4^{(j)} & 0 \\ 0 & 0 & F_4^{(j)} \end{bmatrix},$$

$$\underline{\underline{\mathbb{F}}}_5^{(j)} = \begin{bmatrix} 0 & 0 \\ 0 & 0 \\ 0 & 0 \\ 0 & 0 \\ F_5^{(j)} & F_6^{(j)} \\ 0 & F_5^{(j)} \end{bmatrix}, \underline{\underline{\mathbb{F}}}_6^{(j)} = \begin{bmatrix} 0 \\ 0 \\ 0 \\ 0 \\ 0 \\ F_6^{(j)} \end{bmatrix}, \underline{\underline{G}}^{(j)} = \left[\begin{array}{c|c|c|c|c|c} \underline{\underline{\mathbb{F}}}_1^{(j)} & \underline{\underline{\mathbb{F}}}_2^{(j)} & \underline{\underline{\mathbb{F}}}_3^{(j)} & \underline{\underline{\mathbb{F}}}_4^{(j)} & \underline{\underline{\mathbb{F}}}_5^{(j)} & \underline{\underline{\mathbb{F}}}_6^{(j)} \end{array} \right].$$

Equation (3.14) now becomes

$$\underline{\varepsilon}_1^{(j)} = \underline{\underline{U}}_1 \underline{\underline{G}}^{(j)} \underline{S} + \underline{\underline{V}}_1 \underline{\mathcal{F}}^{(j)} = \underline{\underline{H}}_1^{(j)} \underline{S} + \underline{\underline{V}}_1 \underline{\mathcal{F}}^{(j)}, \tag{3.17}$$

and leads to

$$\underline{\underline{H}}_1^{(j)} \underline{S} = \underline{\varepsilon}_1^{(j)} - \underline{\underline{V}}_1 \underline{\mathcal{F}}^{(j)}, \tag{3.18}$$

where $\underline{\underline{U}}_1 \underline{\underline{G}}^{(j)} = \underline{\underline{H}}_1^{(j)}$.

The manipulations were presented thus far for the strain components at one sensor point location and one loading condition. In the actual experiment, data will be acquired at N sensor point locations for L loading conditions. All this data is now collected in a single set of linear equations

$$\begin{Bmatrix} \underline{\underline{H}}_1^{(1)} \\ \vdots \\ \underline{\underline{H}}_N^{(1)} \\ \hline \underline{\underline{H}}_1^{(2)} \\ \vdots \\ \underline{\underline{H}}_N^{(2)} \\ \hline \vdots \\ \hline \underline{\underline{H}}_1^{(L)} \\ \vdots \\ \underline{\underline{H}}_N^{(L)} \end{Bmatrix} \underline{S} = \begin{Bmatrix} \underline{\varepsilon}_1^{(1)} \\ \vdots \\ \underline{\varepsilon}_N^{(1)} \\ \hline \underline{\varepsilon}_1^{(2)} \\ \vdots \\ \underline{\varepsilon}_N^{(2)} \\ \hline \vdots \\ \hline \underline{\varepsilon}_1^{(L)} \\ \vdots \\ \underline{\varepsilon}_N^{(L)} \end{Bmatrix} - \begin{bmatrix} \underline{\underline{V}}_1 \underline{F}^{(1)} \\ \vdots \\ \underline{\underline{V}}_N \underline{F}^{(1)} \\ \hline \underline{\underline{V}}_1 \underline{F}^{(2)} \\ \vdots \\ \underline{\underline{V}}_N \underline{F}^{(2)} \\ \hline \vdots \\ \hline \underline{\underline{V}}_1 \underline{F}^{(L)} \\ \vdots \\ \underline{\underline{V}}_N \underline{F}^{(L)} \end{bmatrix}, \tag{3.19}$$

recast in a compact manner as

$$\underline{\underline{\mathbb{H}}}\,\underline{S} = \underline{\mathbb{E}} - \underline{\mathbb{V}}. \tag{3.20}$$

Eq. (3.20) represents an over-determined set of linear equations for the 21 entries of the sectional compliance matrix. The solution of this linear system is obtained with the help of singular value decomposition [18] applied to matrix $\underline{\underline{\mathbb{H}}}$,

$$\underline{\underline{\mathbb{H}}} = \check{\underline{\underline{U}}}\,\underline{\underline{\Sigma}}\,\underline{\underline{V}}^T, \tag{3.21}$$

where diagonal matrix $\underline{\underline{\Sigma}}$ stores the singular values and matrices $\underline{\underline{U}}$ and $\underline{\underline{V}}$ are orthogonal matrices, as outlined in appendix A. Substituting eq. (3.21) into eq. (3.20) leads to

$$\check{\underline{\underline{U}}}\,\underline{\underline{\Sigma}}\,\underline{\underline{V}}^T\,\underline{S} = \underline{\mathbb{E}} - \underline{\mathbb{V}}, \tag{3.22}$$

and the 21 components of the sectional compliance matrix are found as

$$\underline{S} = \underline{\underline{V}}\,\underline{\underline{\Sigma}}^{-1}\check{\underline{\underline{U}}}^T\,(\underline{\mathbb{E}} - \underline{\mathbb{V}})\,. \tag{3.23}$$

Chapter 4: Numerical Validation of the Algorithm

To verify the proposed approach, two examples are investigated. The first example is an isotropic aluminum beam and the second is a composite beam made of graphite/epoxy. In both cases, simple models of the beam's cross-sections were developed in *SectionBuilder* given their geometry and material properties and their sectional stiffness properties were evaluated.

As the data reduction algorithm presented in the previous chapter was developed, experimental results from DIC were not available yet. To test the data reduction algorithm, the strain distributions over the outer surface of the beams were computed by *SectionBuilder* for six independent loading conditions and this data was then considered to be "experimental data." To test the robustness of the proposed approach in the presence of measurement noise, a $\pm 10\%$ random scatter was added to the computed strain field and the data reduction algorithm was used with this new strain fields.

4.1 Aluminum Beam Specimen

For the first example, the dimensions of the cross-section are 0.3333×0.0156 ft and is made of aluminum with a Young's modulus 1.439×10^9 lb/ft^2 and Poisson's

ratio 0.33.

Figure 4.1 shows the *SectionBuilder* model of the cross-section and also indicates the sensor point locations on the top and bottom surfaces of the cross-section. *SectionBuilder* generates all the information that appears in eq. (3.12) as well as the strain components at these locations.

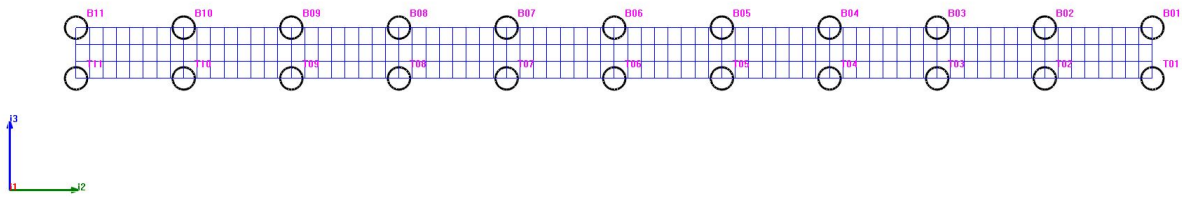

Figure 4.1: Aluminum beam cross-section; symbols (◯) indicate the sensor point locations on top and bottom surfaces.

The sectional compliance matrix evaluated by *SectionBuilder* is

$$\frac{\underline{\underline{\mathcal{S}}}_{SB}}{10^{-7}} = \begin{bmatrix} 1.33 & 0.0 & 0.0 & 0.0 & 0.0 & 0.0 \\ 0.0 & 4.25 & 0.0 & 0.0 & 0.0 & 0.0 \\ 0.0 & 0.0 & 94.4 & 0.0 & 0.0 & 0.0 \\ 0.0 & 0.0 & 0.0 & 44600 & 0.0 & 0.0 \\ 0.0 & 0.0 & 0.0 & 0.0 & 65100 & 0.0 \\ 0.0 & 0.0 & 0.0 & 0.0 & 0.0 & 143 \end{bmatrix}. \tag{4.1}$$

Strain distributions were computed for six independent loading conditions and were used as "experimental data" to drive the proposed data reduction procedure, see eqs. (3.14) to (3.23). The identified sectional compliance matrix, denoted $\underline{\underline{\mathcal{S}}}_{DR}$, was found to be

$$\frac{\underline{\underline{\mathcal{S}}}_{DR}}{10^{-7}} = \begin{bmatrix} 1.33 & 0.0 & 0.0 & 0.0 & 0.0 & 0.0 \\ 0.0 & 4.25 & 0.0 & 0.0 & 0.0 & 0.0 \\ 0.0 & 0.0 & 94.4 & 0.0 & 0.0 & 0.0 \\ 0.0 & 0.0 & 0.0 & 44600 & 0.0 & 0.0 \\ 0.0 & 0.0 & 0.0 & 0.0 & 65100 & 0.0 \\ 0.0 & 0.0 & 0.0 & 0.0 & 0.0 & 143 \end{bmatrix}. \tag{4.2}$$

Good agreement is observed between the sectional compliance matrices computed by *SectionBuilder*, $\underline{\underline{\mathcal{S}}}_{SB}$ see eq. (4.1) and that identified by the proposed data reduction procedure, see eq. (4.2).

Next, the noise expected to be present in measurements was simulated by adding a $\pm 10\%$ random perturbation to the strain fields computed by *SectionBuilder* and the data reduction algorithm was used again with this modified data to identify a new sectional compliance matrix denoted $\underline{\underline{\mathcal{S}}}_{err}$. The relative error matrix, denoted $\underline{\underline{\mathcal{E}}}$, was computed as follows

$$\left[\underline{\underline{\mathcal{E}}}\right]_{i,j} = \frac{\left[\underline{\underline{S}}_{SB}\right]_{i,j} - \left[\underline{\underline{S}}_{err}\right]_{i,j}}{\left[\underline{\underline{S}}_{SB}\right]_{i,j}}.$$

The results obtained with different random perturbations are listed below. The first random perturbation leads to the following sectional compliance matrix

$$\frac{\underline{\underline{\mathcal{S}}}_{err1}}{10^{-7}} = \begin{bmatrix} 1.30 & 0.0 & 0.0 & 0.0 & 0.0 & 0.0 \\ 0.0 & 4.31 & 0.0 & 0.0 & 0.0 & 0.0 \\ 0.0 & 0.0 & 94.4 & 0.0 & 0.0 & 0.0 \\ 0.0 & 0.0 & 0.0 & 44600 & 0.0 & 0.0 \\ 0.0 & 0.0 & 0.0 & 0.0 & 64300 & 0.0 \\ 0.0 & 0.0 & 0.0 & 0.0 & 0.0 & 144 \end{bmatrix}$$

and the associated relative error matrix was found as

$$\mathbf{diag}(\mathcal{E}_1) = \begin{bmatrix} 2.6132\% & -1.5667\% & 0.0261\% & -0.0028\% & 1.2445\% & -0.2152\% \end{bmatrix}$$

The second random perturbation leads to the following sectional compliance matrix

$$\frac{\underline{\underline{\mathcal{S}}}_{err2}}{10^{-7}} = \begin{bmatrix} 1.32 & 0.0 & 0.0 & 0.0 & 0.0 & 0.0 \\ 0.0 & 4.24 & 0.0 & 0.0 & 0.0 & 0.0 \\ 0.0 & 0.0 & 94.4 & 0.0 & 0.0 & 0.0 \\ 0.0 & 0.0 & 0.0 & 44600 & 0.0 & 0.0 \\ 0.0 & 0.0 & 0.0 & 0.0 & 65200 & 0.0 \\ 0.0 & 0.0 & 0.0 & 0.0 & 0.0 & 146 \end{bmatrix}$$

and the associated relative error matrix was found as

$$\mathbf{diag}(\mathcal{E}_2) = \begin{bmatrix} 1.0832\% & 0.2252\% & 0.0068\% & 0.0079\% & -0.2132\% & -1.6107\% \end{bmatrix}$$

Finally, the third random perturbation leads to the following sectional compliance matrix

$$\frac{\underline{\underline{\mathcal{S}}}_{err3}}{10^{-7}} = \begin{bmatrix} 1.33 & 0.0 & 0.0 & 0.0 & 0.0 & 0.0 \\ 0.0 & 4.19 & 0.0 & 0.0 & 0.0 & 0.0 \\ 0.0 & 0.0 & 94.4 & 0.0 & 0.0 & 0.0 \\ 0.0 & 0.0 & 0.0 & 44600 & 0.0 & 0.0 \\ 0.0 & 0.0 & 0.0 & 0.0 & 65700 & 0.0 \\ 0.0 & 0.0 & 0.0 & 0.0 & 0.0 & 138 \end{bmatrix}$$

and the associated relative error matrix was found as

$$\mathbf{diag}(\mathcal{E}_3) = \begin{bmatrix} -0.2415\% & 1.3805\% & -0.0466\% & -0.0338\% & -0.9121\% & 4.2486\% \end{bmatrix}$$

These results indicate that the proposed data reduction algorithm identifies the section compliance matrix within $\pm 5\%$ although a random $\pm 10\%$ perturbation was added to the strain field.

4.2 Composite Beam Specimen

The second example focuses on an anisotropic beam of dimensions 0.25×0.0048 ft made of T300/5208 graphite/epoxy material. The lay-up presents through-the-thickness symmetry with the following sequence, $[0^\circ, +45^\circ, -45^\circ, +30^\circ]_s$, as illus-

trated in fig 4.2. The prorperties of T300/5208 graphite/epoxy are listed in table 4.1.

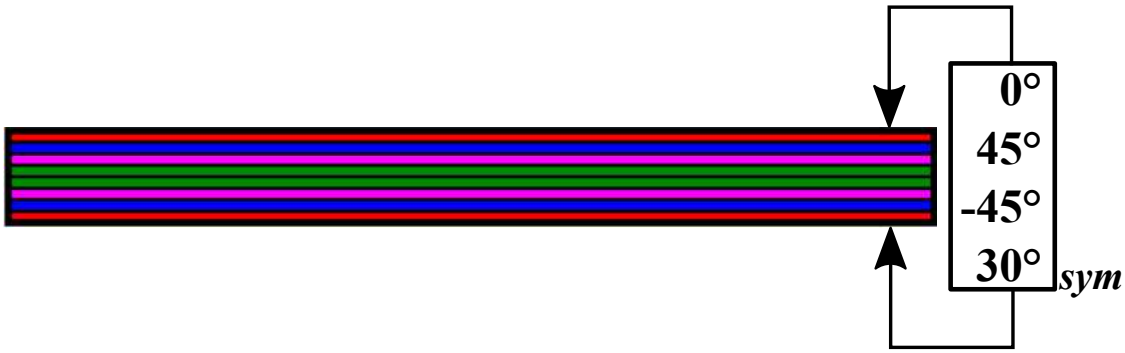

Figure 4.2: Composite beam cross-section with eight plies.

Table 4.1: Properties of T300/5208 graphite/epoxy.

Parameter	**Value**
E_1	3.780×10^9 lb/ft^2
$E_2 = E_3$	2.151×10^8 lb/ft^2
$G_{12} = G_{13}$	1.498×10^8 lb/ft^2
G_{23}	8.087×10^7 lb/ft^2
$\nu_{12} = \nu_{13}$	0.28
ν_{23}	0.33

The compliance matrix computed by *SectionBuilder* is

$$\frac{\underline{\underline{\mathcal{S}}}_{SB}}{10^{-6}} = \begin{bmatrix} 0.54 & 0.15 & 0.0 & 0.0 & 0.0 & 0.0 \\ 0.15 & 1.48 & 0.0 & 0.0 & 0.0 & 0.0 \\ 0.0 & 0.0 & 255 & 0.0 & 0.0 & 0.0 \\ 0.0 & 0.0 & 0.0 & 252000 & -14200 & 0.0 \\ 0.0 & 0.0 & 0.0 & -14200 & 178000 & 0.0 \\ 0.0 & 0.0 & 0.0 & 0.0 & 0.0 & 104 \end{bmatrix}.$$

Note the non-vanishing off-diagonal entries indicating that this beam exhibits extension/shear and bending/torsion elastic couplings.

The sectional compliance matrix identified by the proposed data reduction algorithm was found to be

$$\frac{\underline{\underline{\mathcal{S}}}_{DR}}{10^{-6}} = \begin{bmatrix} 0.54 & 0.15 & 0.0 & 0.0 & 0.0 & 0.0 \\ 0.15 & 1.48 & 0.0 & 0.0 & 0.0 & 0.0 \\ 0.0 & 0.0 & 255 & 0.0 & 0.0 & 0.0 \\ 0.0 & 0.0 & 0.0 & 252000 & -14200 & 0.0 \\ 0.0 & 0.0 & 0.0 & -14200 & 178000 & 0.0 \\ 0.0 & 0.0 & 0.0 & 0.0 & 0.0 & 104 \end{bmatrix}$$

These results are in good agreement with those predicted by *SectionBuilder*.

Here again, the noise expected to be present in measurements was simulated by adding a $\pm 10\%$ random perturbation to the strain fields computed by *SectionBuilder* and the data reduction algorithm was used again with this modified data to identify a new sectional compliance matrix denoted $\underline{\underline{\mathcal{S}}}_{err}$

$$\frac{\underline{\underline{\mathcal{S}}}_{err1}}{10^{-6}} = \begin{bmatrix} 0.54 & 0.15 & 0.0 & 0.0 & 0.0 & 0.0 \\ 0.15 & 1.49 & 0.0 & 0.0 & 0.0 & 0.0 \\ 0.0 & 0.0 & 255 & 0.0 & 0.0 & 0.0 \\ 0.0 & 0.0 & 0.0 & 252000 & -14200 & 0.0 \\ 0.0 & 0.0 & 0.0 & -14200 & 181000 & 0.0 \\ 0.0 & 0.0 & 0.0 & 0.0 & 0.0 & 104 \end{bmatrix}$$

and the associated relative error matrix was found as

$$\underline{\underline{\mathcal{E}}}_1 = \begin{bmatrix} 0.00\% & -1.06\% & 0.0 & 0.0 & 0.0 & 0.0 \\ -1.06\% & -0.74\% & 0.0 & 0.0 & 0.0 & 0.0 \\ 0.0 & 0.0 & 0.00\% & 0.0 & 0.0 & 0.0 \\ 0.0 & 0.0 & 0.0 & 0.00\% & 0.00\% & 0.0 \\ 0.0 & 0.0 & 0.0 & 0.00\% & -1.43\% & 0.0 \\ 0.0 & 0.0 & 0.0 & 0.0 & 0.0 & -0.10\% \end{bmatrix}$$

The second random perturbation leads to the following sectional compliance matrix

$$\frac{\underline{\underline{\mathcal{S}}}_{err2}}{10^{-6}} = \begin{bmatrix} 0.5 & 0.15 & 0.0 & 0.0 & 0.0 & 0.0 \\ 0.15 & 1.46 & 0.0 & 0.0 & 0.0 & 0.0 \\ 0.0 & 0.0 & 25 & 0.0 & 0.0 & 0.0 \\ 0.0 & 0.0 & 0.0 & 252000 & -14200 & 0.0 \\ 0.0 & 0.0 & 0.0 & -14200 & 180000 & 0.0 \\ 0.0 & 0.0 & 0.0 & 0.0 & 0.0 & 104 \end{bmatrix}$$

and the associated relative error matrix was found as

$$\underline{\underline{\mathcal{E}}}_2 = \begin{bmatrix} 0.53\% & -0.36\% & 0.0 & 0.0 & 0.0 & 0.0 \\ -0.36\% & 1.05\% & 0.0 & 0.0 & 0.0 & 0.0 \\ 0.0 & 0.0 & 0.00\% & 0.0 & 0.0 & 0.0 \\ 0.0 & 0.0 & 0.0 & 0.00\% & 0.00\% & 0.0 \\ 0.0 & 0.0 & 0.0 & 0.00\% & -0.84\% & 0.0 \\ 0.0 & 0.0 & 0.0 & 0.0 & 0.0 & -3.32\% \end{bmatrix}$$

Finally, the third random perturbation leads to the following sectional compliance matrix

$$\frac{\underline{\underline{\mathcal{S}}}_{err3}}{10^{-6}} = \begin{bmatrix} 0.53 & 0.15 & 0.0 & 0.0 & 0.0 & 0.0 \\ 0.15 & 1.48 & 0.0 & 0.0 & 0.0 & 0.0 \\ 0.0 & 0.0 & 255 & 0.0 & 0.0 & 0.0 \\ 0.0 & 0.0 & 0.0 & 252000 & -14200 & 0.0 \\ 0.0 & 0.0 & 0.0 & -14200 & 176000 & 0.0 \\ 0.0 & 0.0 & 0.0 & 0.0 & 0.0 & 103 \end{bmatrix}$$

and the associated relative error matrix was found as

$$\underline{\underline{\mathcal{E}}}_3 = \begin{bmatrix} 0.88\% & 2.12\% & 0.0 & 0.0 & 0.0 & 0.0 \\ 2.12\% & 0.09\% & 0.0 & 0.0 & 0.0 & 0.0 \\ 0.0 & 0.0 & 0.00\% & 0.0 & 0.0 & 0.0 \\ 0.0 & 0.0 & 0.0 & 0.00\% & 0.01\% & 0.0 \\ 0.0 & 0.0 & 0.0 & 0.01\% & 1.09\% & 0.0 \\ 0.0 & 0.0 & 0.0 & 0.0 & 0.0 & 0.73\% \end{bmatrix}$$

Clearly, the proposed approach to the measurement of sectional compliance is able to capture the off-diagonal terms of the compliance matrix that correspond to various types of elastic couplings. Although a $\pm 10\%$ random perturbation was added to the strain fields computed by *SectionBuilder*, the proposed data reduction procedure is able to identify the compliance matrix with a far smaller error level. This is due to the use of the singular value decomposition that provides an optimal solution of the highly redundant set of linear equations, see eq. (3.21).

Chapter 5: Conclusion and Future Work

5.1 Conclusion

The knowledge of the sectional stiffness properties of helicopter blades is an indispensable prerequisite to the prediction of their dynamic behavior. Yet, these properties are not measured directly in a reliable manner. Routine static and dynamic tests are often made to estimate the stiffness properties of rotor blade, but these tests measure average stiffness properties over the span of the blade rather that sectional properties. Furthermore, these routine tests cannot identify the off-diagonal terms of the sectional compliance matrix that arise from the presence of elastic couplings in the blade.

This thesis has presented an experimental technique that overcomes these deficiencies. The proposed method aims to measure the complete six-by-six stiffness matrix of helicopter rotor blades made of advanced composite material and presenting arbitrary configurations. The proposed approach combines experimental measurements with a model of the blade's cross-section. The experimental data consists of two independent measurements: *(1)* the sectional loading of the blade measure by a six-axis load cell and *(2)* the strain field over the external surface of the blade obtained from a DIC process. The model of the blade's cross-section is pro-

vided by *SectionBuilder*, a finite element based tool for the analysis of cross-sections of beams of arbitrary configuration made of anisotropic materials. The combination of experimental data and model of the blade's cross-section provides an approach to the determination of its complete sectional compliance matrix. More specifically, this thesis has presented the data reduction procedure that extracts the sectional compliance matrix from the strain fields measure at the outer surface of the blade.

The proposed experimental set-up is under development and hence, actual DIC data was not available to test the proposed data reduction procedure. Consequently, strain distributions over the outer surface of the beams were computed by *SectionBuilder* for six independent loading conditions and this data was then considered to be "experimental data." To test the robustness of the proposed approach in the presence of measurement noise, a $\pm 10\%$ random scatter was added to the computed strain field and the data reduction algorithm was used with this new strain fields.

Three main conclusions can be drawn from this work. First, the proposed data reduction procedure is able to identify the sectional compliance matrix accurately from simulated strain field data. Second, in the presence of noise, the proposed approach still yields reliable predictions of the sectional compliance matrix. In fact the singular value decomposition at the core of the proposed approach is able to extract accurate predictions from the highly redundant data set provided by the strain field. Finally, it was demonstrated that the proposed approach is able to identify the off-diagonal terms of the sectional compliance matrix.

5.2 Future Work

Because the proposed data reduction procedure has been tested with simulated data, the next step of this work is to acquire actual experimental data from DIC and use this data to obtain the sectional compliance matrices of beams with various sectional configurations. Both homogeneous and anisotropic beams with simple geometry will be test first, then the attention should turn to realistic blade configurations.

The proposed experimental procedure should be expanded to be able to deal with full-scale helicopter rotor blades tested in a six-axis testing machine to enable the applications of independent loading conditions. While such instrument would be far more complex and costlier than the present set-up developed at the University of Maryland, the data reduction procedure developed in this thesis would remain unchanged.

Appendix A: The singular value decomposition

The *singular value decomposition theorem* [18] states that an arbitrary, $n \times m$ matrix $\underline{\underline{A}}$ $(n > m)$, of rank r, $r \leq m$ can be decomposed into the following matrix product

$$\underline{\underline{A}}_{(n\times m)} = \underline{\underline{U}}_{(n\times n)} \begin{bmatrix} \underline{\underline{\Sigma}}_{(r\times r)} & \underline{\underline{0}}_{(r\times(m-r))} \\ \underline{\underline{0}}_{((n-r)\times r)} & \underline{\underline{0}}_{((n-r)\times(m-r))} \end{bmatrix} \underline{\underline{V}}^T_{(m\times m)}, \tag{A.1}$$

where $n > m$, $r \leq m$, $\underline{\underline{U}}$ and $\underline{\underline{V}}$ are orthogonal matrices, and $\underline{\underline{\Sigma}} = \mathrm{diag}(\sigma_i)$ a unique diagonal matrix with real, non-negative elements. The other matrices in eq. (A.1) are zero matrices with the corresponding size indicated by their subscript. The elements of $\underline{\underline{\Sigma}}$ are arranged in descending order as

$$\sigma_1 \geq \sigma_2 \geq \sigma_3 \geq \ldots \geq \sigma_r > \sigma_{r+1} = \ldots = \sigma_m = 0, \tag{A.2}$$

where the σ_i are called the *singular values* of $\underline{\underline{A}}$, and, again, $r = \mathrm{rank}(\underline{\underline{A}})$; if $\underline{\underline{A}}$ has *full rank*, $r = m$. Matrices $\underline{\underline{U}}$ and $\underline{\underline{V}}$ can be partitioned as

$$\underline{\underline{U}}_{(n\times n)} = \left[\underline{\underline{\breve{U}}}_{(n\times r)} \quad \underline{\underline{\Gamma}}_{(n\times(n-r))}\right], \text{ and } \underline{\underline{V}}_{(m\times m)} = \left[\underline{\underline{V}}_{1\ (m\times r)} \quad \underline{\underline{V}}_{2\ (m\times(m-r))}\right], \tag{A.3}$$

respectively, and hence, eq. (A.1) can be recast as

$$\underline{\underline{A}}_{(n\times m)} = \left[\underline{\underline{\breve{U}}}_{(n\times r)} \quad \underline{\underline{\Gamma}}_{(n\times(n-r))}\right] \begin{bmatrix} \underline{\underline{\Sigma}}_{(r\times r)} & \underline{\underline{0}}_{(r\times(m-r))} \\ \underline{\underline{0}}_{((n-r)\times r)} & \underline{\underline{0}}_{((n-r)\times(m-r))} \end{bmatrix} \begin{bmatrix} \underline{\underline{V}}^T_{1\,(r\times m)} \\ \underline{\underline{V}}^T_{2\,((m-r)\times m)} \end{bmatrix}, \tag{A.4}$$

where the size of the matrices $\underline{\underline{\check{U}}}$, $\underline{\underline{\Gamma}}$, $\underline{\underline{V}}_1^T$ and $\underline{\underline{V}}_2^T$ are indicated by their subscript. Thus, eq. (A.4) can be simplified to be

$$\underline{\underline{A}} = \underline{\underline{\check{U}}}\,\underline{\underline{\Sigma}}\,\underline{\underline{V}}_1^T, \tag{A.5}$$

i.e., $\underline{\underline{\check{U}}}$ and $\underline{\underline{V}}_1$ are the left and right *singular vectors* of $\underline{\underline{A}}$, respectively. The orthogonality of $\underline{\underline{U}}$ implies the following relationships.

$$\underline{\underline{\check{U}}}\,\underline{\underline{\check{U}}}^T + \underline{\underline{\Gamma}}\,\underline{\underline{\Gamma}}^T = \underline{\underline{I}}, \tag{A.6a}$$

$$\underline{\underline{\check{U}}}^T\underline{\underline{\check{U}}} = \underline{\underline{I}}, \tag{A.6b}$$

$$\underline{\underline{\Gamma}}^T\underline{\underline{\Gamma}}^T = \underline{\underline{I}}, \tag{A.6c}$$

and finally

$$\underline{\underline{\check{U}}}^T\underline{\underline{\Gamma}} = 0, \quad \underline{\underline{\Gamma}}^T\underline{\underline{\check{U}}} = 0. \tag{A.7}$$

Transposing eq. (A.5) and post multiplying by $\underline{\underline{\Gamma}}$ leads to.

$$\underline{\underline{A}}^T\underline{\underline{\Gamma}} = 0, \tag{A.8}$$

where property (A.7) was used; clearly, $\underline{\underline{\Gamma}}$ forms the *null space* of $\underline{\underline{A}}^T$.

When matrix $\underline{\underline{A}}$ has full rank, *i.e.* $r = m$, eq. (A.1) reduces to

$$\underline{\underline{A}} = \underline{\underline{U}}\begin{bmatrix}\underline{\underline{\Sigma}}\\ \underline{\underline{0}}\end{bmatrix}\underline{\underline{V}}^T, \tag{A.9}$$

i.e. the partition of $\underline{\underline{V}}$ is itself, and eq. (A.9) simplifies to

$$\underline{\underline{A}} = \underline{\underline{\check{U}}}\,\underline{\underline{\Sigma}}\,\underline{\underline{V}}^T \tag{A.10}$$

Bibliography

[1] A.R. Atilgan and D.H. Hodges. Unified nonlinear analysis for nonhomogeneous anisotropic beams with closed cross-sections. *AIAA Journal*, 29(11):1990–1999, November 1991.

[2] A.R. Atilgan, D.H. Hodges, and M.V. Fulton. Nonlinear deformation of composite beams: Unification of cross-sectional and elastica analyses. *Applied Mechanics Reviews*, 44(11):S9–S15, November 1991.

[3] O.A. Bauchau. *Flexible Multibody Dynamics*. Springer, Dordrecht, Heidelberg, London, New-York, 2011.

[4] O.A. Bauchau and J.I. Craig. *Structural Analysis with Application to Aerospace Structures*. Springer, Dordrecht, Heidelberg, London, New-York, 2009.

[5] O.A. Bauchau and S.L. Han. Three-dimensional beam theory for flexible multibody dynamics. *Journal of Computational and Nonlinear Dynamics*, 9(4):041011 (12 pages), 2014.

[6] V.L. Berdichevsky. On the energy of an elastic rod. *Prikladnaya Matematika y Mekanika*, 45(4):518–529, 1982.

[7] M. Borri, G.L. Ghiringhelli, and T. Merlini. Linear analysis of naturally curved and twisted anisotropic beams. *Composites Engineering*, 2(5-7):433–456, 1992.

[8] N. Buannic and P. Cartraud. Higher-order effective modeling of periodic heterogeneous beams. I. Asymptotic expansion method. *International Journal of Solids and Structures*, 38(40-41):7139–7161, 2001.

[9] N. Buannic and P. Cartraud. Higher-order effective modeling of periodic heterogeneous beams. II. Derivation of the proper boundary conditions for the interior asymptotic solution. *International Journal of Solids and Structures*, 38(40-41):7163–7180, 2001.

[10] J. C.-B. de Saint-Venant. Mémoire sur la torsion des prismes. *Receuil des Savants Étrangers*, 14:233–560, 1855.

[11] J. C.-B. de Saint-Venant. Mémoire sur la flexion des prismes. *Journal de Mathématiques de Liouville*, 1:89–189, 1856.

[12] S.B. Dong, J.B. Kosmatka, and H.C. Lin. On Saint-Venant's problem for an inhomogeneous, anisotropic cylinder-Part I: Methodology for Saint-Venant solutions. *Journal of Applied Mechanics*, 68(3):376–381, 2001.

[13] A.N. Druz, N.A. Polyakov, and Y.A. Ustinov. Homogeneous solutions and Saint-Venant problems for a naturally twisted rod. *Journal of Applied Mathematics and Mechanics*, 60(4):657–664, 1996.

[14] A.N. Druz and Y.A. Ustinov. Green's tensor for an elastic cylinder and its applications in the development of the Saint-Venant theory. *Journal of Applied Mathematics and Mechanics*, 60(1):97–104, 1996.

[15] R. El Fatmi and H. Zenzri. On the structural behavior and the Saint-Venant solution in the exact beam theory: Application to laminated composite beams. *Computers & Structures*, 80(16-17):1441–1456, 2002.

[16] R. El Fatmi and H. Zenzri. A numerical method for the exact elastic beam theory. Applications to homogeneous and composite beams. *International Journal of Solids and Structures*, 41(9-10):2521–2537, 2004.

[17] V. Giavotto, M. Borri, P. Mantegazza, G. Ghiringhelli, V. Carmaschi, G.C. Maffioli, and F. Mussi. Anisotropic beam theory and applications. *Computers & Structures*, 16(1-4):403–413, 1983.

[18] G.H. Golub and C.F. van Loan. *Matrix Computations*. The Johns Hopkins University Press, Baltimore, second edition, 1989.

[19] S.L. Han and O.A. Bauchau. Nonlinear three-dimensional beam theory for flexible multibody dynamics. *Multibody System Dynamics*, 34(3):211–242, July 2015.

[20] S.L. Han and O.A. Bauchau. On Saint-Venant's problem for helicoidal beams. *Journal of Applied Mechanics*, 83(2):021009 (14 pages), 2016.

[21] P. Hariharan. *Basics of Interferometry*. Elsevier, Amsterdam, second edition, 2007.

[22] D.H. Hodges. *Nonlinear Composite Beam Theory*. AIAA, Reston, Virginia, 2006.

[23] K. Hoffmann. *An Introduction to Measurements using Strain Gages*. Hottinger Baldwin Messtechnik GmbH, Darmstadt, 1989.

[24] D. Ieşan. Saint-Venant's problem for inhomogeneous and anisotropic elastic bodies. *Journal of Elasticity*, 6(3):277–294, 1976.

[25] D. Ieşan. On Saint-Venant's problem. *Archive for Rational Mechanics and Analysis*, 91(4):363–373, 1986.

[26] J. S. Kim, M. Cho, and E. C. Smith. An asymptotic analysis of composite beams with kinematically corrected end effects. *International Journal of Solids and Structures*, 45(7-8):1954–1977, 2008.

[27] J.B. Kosmatka, H.C. Lin, and S.B. Dong. On Saint-Venant's problem for an inhomogeneous, anisotropic cylinder-Part II: Cross-sectional properties. *Journal of Applied Mechanics*, 68(3):382–391, 2001.

[28] P. Ladevèze and J. Simmonds. New concepts for linear beam theory with arbitrary geometry and loading. *European Journal of Mechanics - A/Solids*, 17(3):377–402, 1998.

[29] S.G. Lekhnitskii. *Theory of Elasticity of an Anisotropic Body*. MIR Publishers, Moscow, second edition, 1977.

[30] H.C. Lin, J.B. Kosmatka, and S.B. Dong. On Saint-Venant's problem for an inhomogeneous, anisotropic cylinder-Part III: End effects. *Journal of Applied Mechanics*, 68(3):392–398, 2001.

[31] A.E.H. Love. *A Treatise on The Mathematical Theory of Elasticity*. Dover Publications, Inc., New York, fourth edition, 1944.

[32] A. Mielke. Saint-Venant's problem and semi-inverse solutions in nonlinear elasticity. *Archive of Rational Mechanics and Analysis*, 102:205–229, 1988.

[33] A. Mielke. Normal hyperbolicity of center manifolds and Saint-Venant's principle. *Archive of Rational Mechanics and Analysis*, 110:353–372, December 1990.

[34] M. Morandini, M. Chierichetti, and P. Mantegazza. Characteristic behavior of prismatic anisotropic beam via generalized eigenvectors. *International Journal of Solids and Structures*, 47:1327–1337, 2010.

[35] M.A. Sutton, J.J. Orteu, and H.W. Schreier. *Image Correlation for Shape, Motion and Deformation Measurements: Basic Concepts, Theory and Applications*. Springer, New York, 2009.

[36] S.P. Timoshenko and J.N. Goodier. *Theory of Elasticity*. McGraw-Hill Book Company, New York, third edition, 1970.

[37] L.N. Trollinger. Refined performance and loads of a mach-scale rotor at high advance ratios. Master's thesis, University of Maryland, College Park, College Park, MD, September 2017.

[38] Y. A. Ustinov. Solutions of the Saint-Venant problem for a cylinder with helical anisotropy. *Journal of Applied Mathematics and Mechanics*, 67(1):89–98, 2003.

[39] W.B. Yu, D.H. Hodges, V.V. Volovoi, and C.E.S. Cesnik. On Timoshenko-like modeling of initially curved and twisted composite beams. *International Journal of Solids and Structures*, 39(19):5101–5121, 2002.

[40] W.X. Zhong. Plane elasticity problem in strip domain and Hamiltonian system. *Journal of Dalian University of Technology*, 4:373–384, 1991.

[41] W.X. Zhong. *A New Systematic Methodology for Theory of Elasticity*. Dalian University of Technology Press, Dalian, 1995.